Materials Advances

ROYAL SOCIETY OF CHEMISTRY

PAPER

View Article Online
View Journal | View Issue

Cite this: *Mater. Adv.*, 2026, 7, 3627

Harnessing the zinc(II) bis-terpyridine complex to overcome drug resistance: mechanistic insights into antibacterial activity

Sourav Sutradhar, †[a] Saurabh Gupta,†[b] Parnashabari Sarkar,[a] Dipankar Das,[a] Kamaldeep Paul *[bc] and Biswa Nath Ghosh *[a]

The increasing prevalence of drug-resistant bacteria represents a serious global health challenge, prompting scientists to develop innovative antibacterial compounds. An example of such a compound with significant potential as an antibacterial agent is zinc(II) complex **ZnL_2** of a terpyridine-based ligand 4′-(3,4-diethoxyphenyl)-2,2′:6′,2″-terpyridine **L**. The single crystal X-ray diffraction analysis of **$[ZnL_2](ClO_4)_2{\cdot}CH_3CN{\cdot}H_2O$** confirms distorted octahedral coordination geometry around zinc(II) in which zinc is coordinated by two terpyridine ligands **L**. The preliminary investigations identified **ZnL_2** as a potent antibacterial compound, outperforming widely used antibiotics like amoxicillin, tetracycline, and chloromycin in its action against *Bacillus subtilis* and *Salmonella enterica*. The complex **ZnL_2** efficiently inhibits the development of drug resistance, with 20 passages for *B. subtilis* and 23 passages for *S. enterica*, and showed low toxicity towards normal cell lines of Hek293. As part of the extended investigation, biofilm inhibition, membrane disruption, leakage, and intracellular oxidative stress assays were done. Further analysis of the complex's interactions with DNA was conducted to assess its potential for targeting bacterial DNA as a therapeutic agent. The interaction of the complex with transport proteins such as serum albumin was evaluated to gain an initial understanding of the drug's ADME characteristics. The findings of this study emphasise the substantial antibacterial potential of the developed zinc terpyridine complex. Its promising activity could form the basis for future advancement in the treatment of bacterial infections.

Received 16th May 2025,
Accepted 13th February 2026

DOI: 10.1039/d5ma00502g

rsc.li/materials-advances

1. Introduction

Nitrogen-based heterocyclic compounds have received significant attention due to their extensive range of applications in pharmacology.[1,2] Nitrogen-containing heterocycles, including pyridine, pyrimidine, quinoline, and pyrazine, are fundamental structural elements in many phytochemical drugs like codeine, morphine, vinblastine, reserpine, procaine, papaverine, emetine, and digitalis-derived cardiac glycosides.[3] These heterocycles are also extensively found in synthetic drugs such as diazepam, isoniazid, chlorpromazine, metronidazole, chloroquine, azidothymidine, antipyrine, *etc.*[3–5] In addition, most enzymes, co-enzymes, hormones, vitamins, nucleic acids and alkaloids have *N*-heterocyclic skeletons.[5] 2,2′:6′,2″-Terpyridines are one such category of nitrogen-based heterocyclic ligands, which have been used extensively as anticancer,[6] antioxidant[7] and antimicrobial agents.[8] These ligands have high affinity for binding with biomolecules like serum albumin and DNA. In addition, 2,2′:6′,2″-terpyridines also possess strong binding affinity towards transition metals, due to the presence of three pyridine ring nitrogen atoms. The metal complexes of 2,2′:6′,2″-terpyridines have significant applications in anion and amino acid sensing,[9–11] halogen bonding,[12,13] gelation,[14–17] dye-sensitised solar cells,[18,19] catalytic fields,[11] *etc.* Among the various transition metal complexes, zinc complexes are of significant interest. Zinc is the second most abundant trace element in the human body, playing a crucial role in maintaining health across all life stages and catalyzes over 300 enzymes, facilitating critical biochemical processes.[20] The zinc(II) ion does not participate in oxidation–reduction reactions but its role in metalloenzymes is attributed to its ability to act as a Lewis acid.[21] Zinc complexes have been studied for various applications in radioprotection, tumor photosensitizers, antidiabetic agents, anticonvulsants, and anti-inflammatory agents.[22] Zinc complexes can also bind with

[a] *Department of Chemistry, National Institute of Technology Silchar, Silchar, Assam, India. E-mail: bnghosh@che.nits.ac.in*
[b] *TIET-VT, Centre of Excellence in Emerging Materials, Thapar Institute of Engineering and Technology, Patiala, Punjab, India 147004*
[c] *Department of Chemistry and Biochemistry, Thapar Institute of Engineering and Technology, Thapar, Punjab, India. E-mail: kpaul@thapar.edu*
† Equally contributed.

serum albumins and DNA, and thus have potential anticancer activity. In the development of newer antibiotics to overcome the resistance of microbes, zinc complexes have shown promising results against bacteria and fungi, demonstrating potential antimicrobial activity.[23] The escalating prevalence of multi-drug-resistant microorganisms, a direct consequence of antibiotic overuse and misuse, poses a significant threat to global health and socioeconomic stability.[24] The inability of current antibiotics to effectively combat these infections underscores the importance of developing novel antibacterial agents.[25] Despite decades of research, the development of such agents remains a pressing challenge. Among all bacteria accountable for deadly diseases, the treatment of infections caused by *Bacillus subtilis* and *Salmonella enterica* has caused a major challenge. *B. subtilis* is generally considered non-pathogenic and is widely utilized in industrial and probiotic applications. However, certain strains can pose health risks, particularly to immunocompromised individuals. In rare instances, *B. subtilis* has been associated with serious infections such as bacteremia, meningitis, and cerebral abscesses.[26] Similarly, *S. enterica* is a major cause of foodborne illnesses worldwide. It is divided into numerous serotypes, many of which are associated with various health issues in humans and animals.[27] Salmonellosis is the most common illness caused by *S. enterica*. Typhoid fever, paratyphoid fever, and chronic carrier state are also caused by *S. enterica.*[28] Considering the urgency for innovative therapeutic approaches and to address this critical public health concern in the form of antibiotic resistance, a zinc(II) complex of the terpyridine ligand has been examined against bacterial strains in search of a drug as an antibacterial agent.

1.1 Designing of the work

Limited work has been done on antibacterial activity against *B. subtilis* and *S. enterica*, and a comprehensive mechanistic evaluation has not been done with any antibacterial agent against both bacterial strains. Over the past few years, researchers have developed many zinc complexes of different ligands. These reported complexes exhibited antibacterial activity against *B. subtilis* with MIC value >10 μg mL^{-1}; also they showed their antibacterial potential towards other bacterial strains such as *E. coli*, *S. aureus*, *E. faecalis*, and *P. aeruginosa*, but up to now no zinc complexes have been reported that exhibit excellent antibacterial activity against *B. subtilis* and *S. enterica* with low MIC values (Table S1). Moreover, the antibacterial activity of terpyridine zinc complexes has not been explored in depth so far. To address the limited exploration of the antibacterial activity of terpyridine zinc complexes and to fill up this gap, we have synthesised a more drug resistant and less toxic zinc terpyridine complex. Here, in this work, we have synthesized zinc(II) complex $\mathbf{ZnL_2}$ of 4′-(3,4-diethoxyphenyl)-2,2′:6′,2″-terpyridine ligand **L** in a 1 : 2 ratio (Scheme 1). The zinc complex $\mathbf{ZnL_2}$ has been characterized by NMR, UV-vis, HRMS, and SC-XRD studies. The prepared $\mathbf{ZnL_2}$ has been examined for antibacterial potential against four Gram-positive and four Gram-negative bacterial strains. It showed good antibacterial activity against *B. subtilis* and *S. enterica* with low MIC values of 1.56 μg mL^{-1} and outperformed the marketed drugs and was further assessed for its mode of action *via* membrane disruption, protein leakage, biofilm inhibition, metabolic dysfunction, oxidative stress damage, and lipid peroxidation. The interaction of $\mathbf{ZnL_2}$ with calf thymus (ct)-DNA was also studied with spectroscopic techniques to build DNA-targeting antibacterial agents. Furthermore, the binding behavior of $\mathbf{ZnL_2}$ with human serum albumin (HSA), a transportation protein, was explored to obtain initial information about the drug's ADME (absorption, distribution, metabolism, and excretion) properties.

2. Results and discussion

2.1 Chemistry

The ligand 4′-(3,4-diethoxyphenyl)-2,2′:6′,2″-terpyridine **L** was synthesized by the reaction of two equivalents of 2-acetylpyridine and one equivalent of 3,4-diethoxybenzaldehyde in ammonia and methanolic KOH medium, according to the literature method.[29] The addition of $NaClO_4$ to a stirred reaction mixture of $Zn(NO_3)_2{\cdot}6H_2O$ (1 equivalent) and **L** (2 equivalents) in MeOH afforded the yellow coloured zinc complex $\mathbf{ZnL_2}$ (Scheme 1). **L** and the complex $\mathbf{ZnL_2}$ were characterized by NMR, UV-visible, HRMS and FTIR analyses (Fig. S1–S7 in SI). The UV-visible absorption spectra of the zinc complex in acetonitrile show absorption peaks at 230 nm, 277 nm

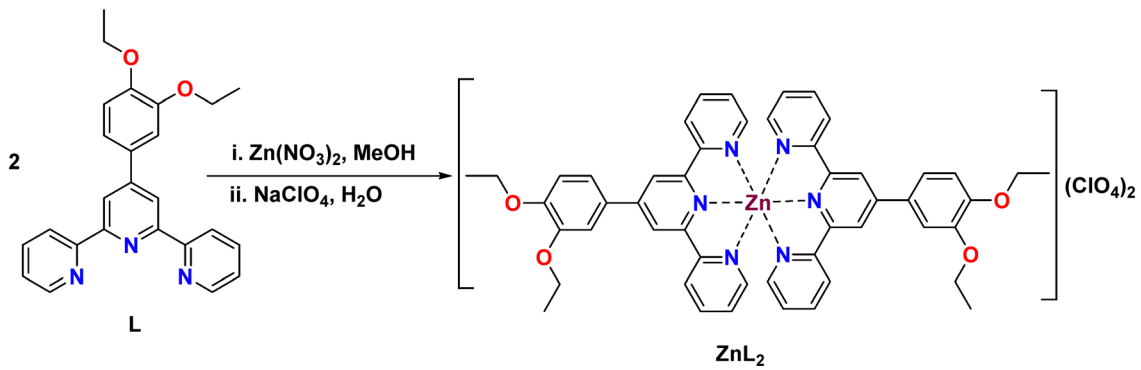

Scheme 1 Schematic diagram for synthesis of zinc complex $\mathbf{ZnL_2}$.

($\pi \rightarrow \pi^*$ transition), and 322 nm (attributed to metal-induced intra-ligand charge transfer).[29] In HRMS, the molecular ion peak at m/z 959.2336 corresponds to $[\mathbf{ZnL_2}](ClO_4)^+$. The zinc complex has also been characterized by X-ray single crystal diffraction study. The stability of $\mathbf{ZnL_2}$ was measured by UV-visible spectroscopy in PB buffer at pH 7.4. The $\mathbf{ZnL_2}$ spectral peaks remained unchanged, apart from a slight variation in intensity after 48 hours at room temperature (Fig. S8).

2.2 Crystal structure of the zinc(II) complex

Yellow-coloured single crystals of the zinc complex were obtained by slow diffusion of di-isopropyl ether into an acetonitrile–methanol (1 : 1) solution of the complex. The complex was crystallized in the monoclinic ($P2_1/n$) space group. X-ray crystallographic data and structural refinement parameters for the complex are reported in Table S2. The crystal structure of the complex consists of a $[Zn(\mathbf{L})_2]^{2+}$ cation (Fig. 1), two perchlorate anions, one solvated water molecule, and one solvated acetonitrile molecule. The crystal structure of the zinc complex confirms the anticipated 1 : 2 metal to ligand stoichiometry in the cation. The dicationic charge on the complex is balanced by the presence of two perchlorates as counter anions. The zinc ion in the crystal structure shows a distorted octahedral geometry, bound by six pyridine nitrogen atoms of two ligands to give a ZnN_6 type coordinated complex with meridional configuration. The central Zn–N bond distances [2.069(5)–2.082(5) Å] are shorter than terminal Zn–N bond distances [2.161(5)–2.204(5) Å] due to the restricted bite angle of the terpyridine core moiety. There is a slight deviation from the ideal octahedral geometry, as evidenced by the bond angle around the zinc ion [N2–Zn1–N5 171.8(2)°]. Selected bond distances and angles are presented in Table S3. Similar bond distances were observed in the previously reported zinc–terpyridine complexes.[30,31] The central pyridine ring is attached to diethoxyphenyl showing a slight deviation from planarity with dihedral angles in the range of 7.9(10)–14.2(11)°. In $\mathbf{ZnL_2}$ it is observed that on one side of the ligand **L**, the central pyridine ring remains coplanar with both the terminal pyridine rings, while the other side of the ligand **L** is slightly tilted by a dihedral angle range of 5.9(11)–12.7(10)°. Three of the ethoxy groups remain coplanar with the phenyl, but one ethoxy group O3–C47–C48 is out of plane. The dihedral angles around the zinc ions for $\mathbf{ZnL_2}$ are N1–C5–C6–N2 = 3.6(8)°, N2–C16–C17–N3 = 1.4(8)°, N4–C30–C31–N5 = 6.8(8)°, and N5–C41–C42–N6 = 7.9(8)°.

2.3 Quantum chemical studies

Quantum chemical studies are used to forecast the important pharmacokinetic features and the feasibility of building important interactions with target molecules.[32,33] FMO (frontier molecular orbitals) control the interactions between molecules and target sites, and the energy difference between HOMO and LUMO aids in determining a compound's bioactivity. The HOMO and LUMO exert a positive influence on the ligand–receptor interaction process.[33] The ligand and $\mathbf{ZnL_2}$ displayed energy gaps of 4.221 and 0.556 eV, respectively, indicating that both can exert good bioactivity (Table 1). The HOMO of the ligand is located on the phenyl ring attached with two ethoxy groups, manifesting that it interacts *via* electrostatic interactions with positively charged biological ions, and the LUMO of the ligand is located over the whole of the ligand, indicating that it binds with negatively charged residues. In the case of $\mathbf{ZnL_2}$, both HOMO and LUMO are located over the whole complex, indicating that the whole complex binds with negative as well as positively charged biological ions. The Cartesian coordinates of **L** and $\mathbf{ZnL_2}$ are given in Tables S4 and S5, respectively.

2.4 *In vitro* antibacterial activity

Using a two-fold serial dilution procedure as recommended by CLSI (Clinical and Laboratory Standards Institute), the ligand **L** and its zinc metal complexes in 1 : 1 (Zn**L**) and 1 : 2 ($\mathbf{ZnL_2}$) ratio were evaluated for their ability to suppress bacterial growth.[34,35] The ligand and complexes were tested against Gram-positive and Gram-negative bacterial strains, including *Bacillus subtilis*, *Enterococcus faecalis*, *Listeria species*, and *Staphylococcus aureus*, as well as *Salmonella enterica*, *Escherichia coli*, *Serratia marcescens*, and *Acinetobacter calcoaceticus*. As represented in Table 2, the ligand displayed moderate activity in inhibiting the growth of most of the tested bacterial strains. When the ligand was complexed with the zinc salt in the form of mono-complex Zn**L**, it exhibited better activity in suppressing the growth of most of the tested bacterial strains. This might be due to the change in the electron density of the ligand when complexed with $Zn(NO_3)_2$. The free nitrate group helped to increase the water solubility of the complex due to which it was able to exhibit

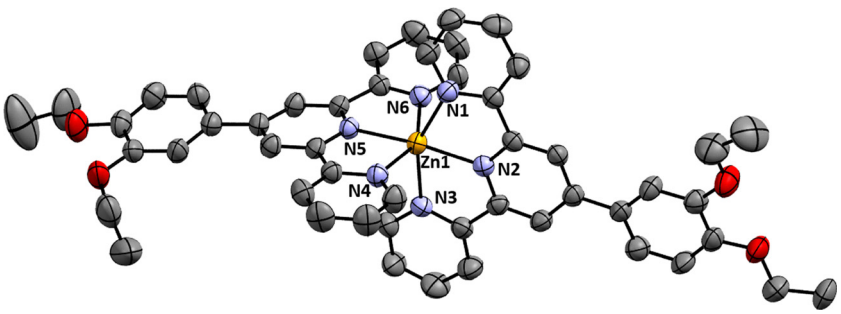

Fig. 1 Crystal structures of the zinc complex $\mathbf{ZnL_2}$. Hydrogen atoms, counter anions and solvent molecules are omitted for clarity.

Table 1 Atomic orbital HOMO–LUMO compositions of the ligand and the **ZnL_2** complex

Compound	HOMO (eV)	LUMO (eV)	ΔE (eV)
Ligand	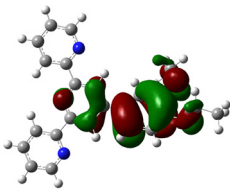 E = -5.950	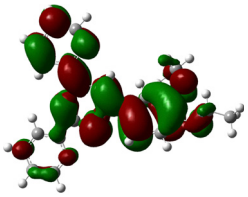 E = -1.729	4.221
ZnL_2	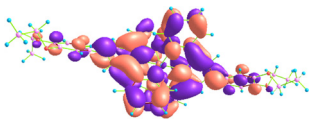 E = -2.645	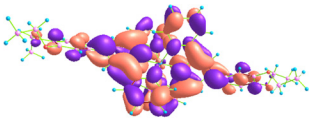 E = -2.089	0.556

Table 2 Antibacterial activity data as MIC (μg mL^{-1}) for ligand **L** and complexes Zn**L** and **ZnL_2**

	Gram-positive bacterial strains				Gram-negative bacterial strains			
Comp.	*E. faecalis*	*B. subtilis*	*L. species*	*S. aureus*	*E. coli*	*S. enterica*	*A. calcoaceticus*	*S. marcescens*
Ligand	50	25	50	12.5	50	100	12.5	25
Zn**L**	12.5	3.12	12.5	1.56	25	12.5	25	6.25
[**ZnL_2**] $(ClO_4)_2$	3.12	1.56	6.25	3.12	6.25	1.56	3.12	3.12
[**ZnL_2**] Cl_2	3.12	1.56	6.25	3.12	6.25	1.56	3.12	3.12
[**ZnL_2**] $(NO_3)_2$	3.12	1.56	6.25	3.12	6.25	1.56	3.12	3.12
[**ZnL_2**]SO_4	3.12	1.56	6.25	3.12	6.25	1.56	3.12	3.12
A	6.25	50	50	25	100	200	50	1.56
B	3.12	1.56	6.25	1.56	1.56	100	1.56	1.56
C	3.12	1.56	1.56	3.12	3.12	50	3.12	1.56
D	50	6.25	6.25	100	12.5	50	6.25	25

A – amoxicillin; B – tetracycline; C – chloromycin; D – colistin.

better antibacterial properties than the ligand itself. Complex Zn**L** inhibited the growth of all the tested bacterial strains with MIC values ranging from 3.12 to 25 μg mL^{-1}. The activity of Zn**L** was enhanced further when the free nitrate group was replaced with the same ligand, thus forming a complex of zinc and the ligand in 1 : 2 ratio. **ZnL_2** with perchlorate ion as the counter ion exhibited excellent activity in suppressing the growth of the tested bacterial strains, with MIC values ranging from 1.56 to 6.25 μg mL^{-1}, which were far superior to those of Zn**L**. The enhanced antibacterial activity of **ZnL_2** may be attributed to the presence of two electron-donating ligands attached to Zn, which increases the overall electron density of [**ZnL_2**] $(ClO_4)_2$. Thus, it has been found that the free ligand exhibited moderate activity, Zn**L** displayed better activity than the ligand, whereas [**ZnL_2**] $(ClO_4)_2$ exhibited excellent activity in inhibiting the growth of bacterial strains. The results were also compared to marketed drugs amoxicillin, tetracycline, chloromycin, and colistin, where [**ZnL_2**] $(ClO_4)_2$ outperformed these marketed drugs. Comparison of the results of [**ZnL_2**] $(ClO_4)_2$ with those of the modern membrane-targeting drug colistin showed that [**ZnL_2**] $(ClO_4)_2$ remarkably outperformed colistin in inhibiting the growth of all the tested strains. Furthermore, to determine whether the antibacterial activity of the [**ZnL_2**] $(ClO_4)_2$ complex arises primarily from the metal–ligand framework and is independent of the counterion, the **ZnL_2** complex was also evaluated with clinically accepted counterions, including Cl^-, NO_3^- and SO_4^{2-}. The results showed no significant change in antibacterial activity upon replacement of the perchlorate ion with these alternative anions, indicating that the observed antibacterial effect is intrinsic to the **ZnL_2** complex and not influenced by the nature of the counterion. Based on this counterion-independent antibacterial performance, [**ZnL_2**] $(ClO_4)_2$ was selected for further detailed investigations. Subsequent studies focused on evaluating its antibacterial efficacy and elucidating its preliminary mechanism of action against *Bacillus subtilis* and *Salmonella enterica*, in view of its potent ability to inhibit bacterial growth.

2.5 Bactericidal or bacteriostatic action

To ascertain whether the mode of action displayed by active **ZnL_2** towards *B. subtilis* and *S. enterica* is bacteriostatic or bactericidal, minimal bacterial concentrations (MBCs) were investigated following the completion of preliminary experiments. The active **ZnL_2** displayed MBC/MIC values of 2 and 1 against *B. subtilis* and *S. enterica*, respectively (Fig. 2a),

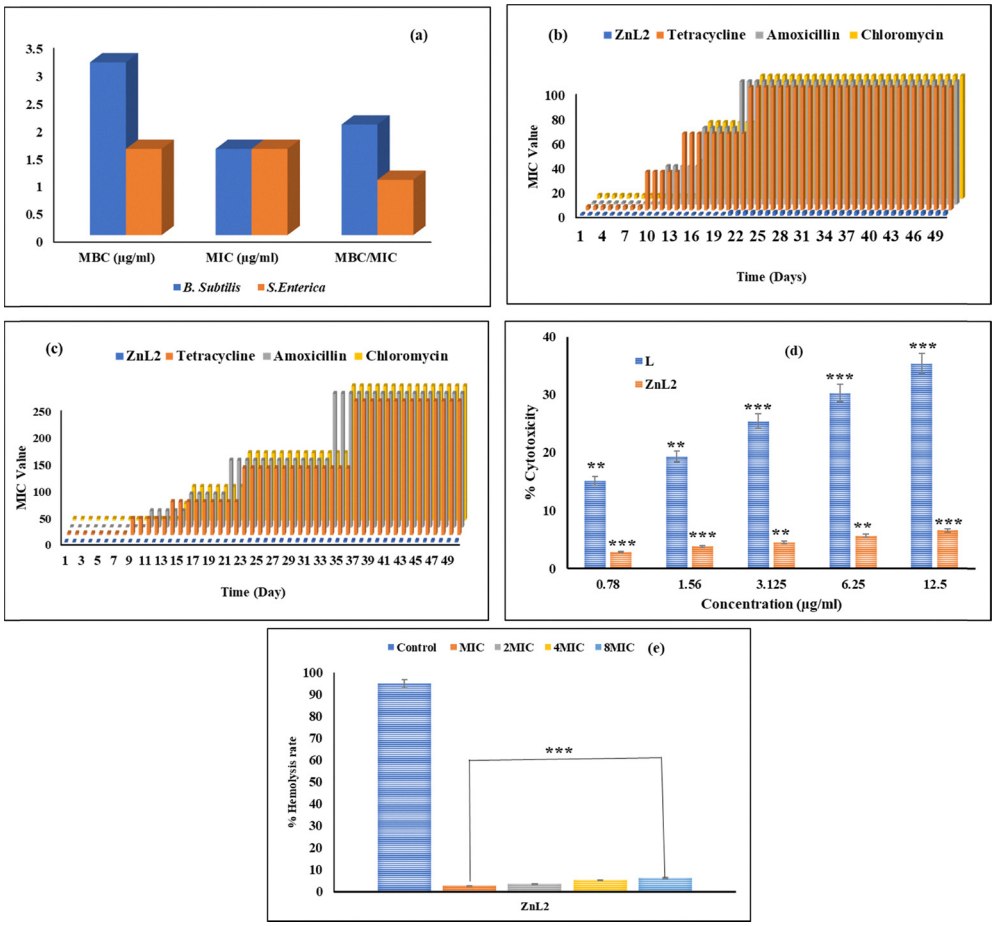

Fig. 2 (a) Evaluation of MBC and MIC values of $\mathbf{ZnL_2}$; bacterial susceptibility evaluation of $\mathbf{ZnL_2}$, tetracycline, amoxicillin, and chloromycin towards (b) *B. subtilis* and (c) *S. enterica*; (d) cytotoxicity of $\mathbf{ZnL_2}$ towards normal cell line Hek293 and (e) hemolysis rate of compounds **8e** and **8h** against red blood cells. $^{*}P < 0.05$; $^{**}P < 0.01$; $^{***}P < 0.001$. $n = 3$.

suggesting that the complex is bactericidal to both the tested bacterial strains.

2.6 Bacterial susceptibility evaluation

Antibiotic abuse has made treating bacterial illnesses extremely difficult since it has led to the development of bacterial resistance, which has reduced the effectiveness of present drugs and increased their dosage.[36–38] Using tetracycline, amoxicillin, and chloromycin as positive controls, the drug resistance of $\mathbf{ZnL_2}$ was investigated at the MIC value against *B. subtilis* and *S. enterica* in up to 25 passages. According to the data shown in Fig. 2b and c, $\mathbf{ZnL_2}$ was found to be more effective than commercial antibiotics at delaying the onset of drug resistance against both the tested strains. The MIC values of tetracycline, amoxicillin, and chloromycin increased significantly after 9, 11, and 15 passages, respectively, whereas $\mathbf{ZnL_2}$ did not show any discernible change in MIC values until 20 passages against *B. subtilis*. Compared to this, in the case of *S. enterica*, $\mathbf{ZnL_2}$ delayed the occurrence of drug resistance up to 23 passages, while the MIC of marketed drugs tetracycline, amoxicillin, and chloromycin enhanced dramatically after 7, 10, and 13 passages, respectively. These results suggest that $\mathbf{ZnL_2}$ can overcome resistance in treating infections due to its low potential for generating drug resistance in *B. subtilis* and *S. enterica.*

2.7 Cytotoxic studies of the complex

A key component of the drug candidate to develop as an antibacterial agent is its biosafety, which is evaluated by determining the cytotoxicity of the active drug candidates towards normal cell lines.[39] Thus, MTT assay was employed to evaluate the cytotoxic effect of active drug candidate $\mathbf{ZnL_2}$ against normal cell line Hek293. At several doses ranging from 0.78 to 12.5 μg mL^{-1}, $\mathbf{ZnL_2}$ exhibited only 2.81, 3.85, 4.53, 5.63 and 6.57% cytotoxicity towards normal cell line Hek293 (Fig. 2d). Also, we have evaluated the cytotoxicity of the free ligand towards normal cell lines to understand whether Zn(II) coordination improves the properties compared to the free ligand. The result suggested that the free ligand at various concentrations exhibited 15.2 to 35.4% cytotoxicity towards Hek293, indicating the decreased therapeutic value of the free ligand. Comparing the cytotoxicity results of the free ligand and $\mathbf{ZnL_2}$, the complex displayed very low toxicity to normal cell lines compared to the free ligand. The low cytotoxicity of $\mathbf{ZnL_2}$ to normal cells over bacterial cells suggested the biosafety of the complex and its potential for further research and

development into antibacterial drugs. The cytotoxic experiment was conducted in triplicate.

An essential parameter in evaluating the biosafety of synthesized **ZnL_2** is its propensity to induce hemolysis. In view of this, we examined the hemolytic activity of complex **ZnL_2** against goat red blood cells (RBCs) at various concentrations (MIC, 2 × MIC, 4 × MIC, and 8 × MIC), with Triton X-100 serving as the positive control. As depicted in Fig. 2e, **ZnL_2** maintained remarkably low hemolysis rates, which remained below 7% even after 3 h of exposure. Notably, at the highest tested concentration of 8 × MIC, complex **ZnL_2** induced hemolysis of only 6.2%. These values are well within the acceptable threshold for hemocompatible agents, underscoring its biosafety profile. The absence of significant RBC lysis in the presence of active complex **ZnL_2** highlights its therapeutic potential. This assay was conducted in triplicate to ensure reproducibility and statistical reliability.

2.8 Kinetics of bactericidal activity

The strong bactericidal effects of antibiotics inhibit the development of bacterial resistance. Therefore, a key test for determining the drug's bactericidal qualities at various concentrations is the time–kill kinetic study.[40,41] Within three hours, *B. subtilis* and *S. enterica* in the control inoculum entered their exponential phase (Fig. 3a and b), whereas the growth of bacteria was inhibited and cells were destroyed upon treatment with **ZnL_2** inoculum. Within 4.5 and 3.5 h at MIC, **ZnL_2** began to exhibit its bactericidal activity against *B. subtilis* and *S. enterica*, respectively. At higher concentrations of **ZnL_2**, such as 2 × MIC, 4 × MIC, and 8 × MIC, the time needed to kill bacteria in the inoculum decreased from 4.5 h to 3 h in the case of *B. subtilis* and from 3.5 to 1.5 h in the case of *S. enterica.* Consequently, **ZnL_2** had outstanding bactericidal activities in addition to good antibacterial properties, which shortened the treatment period.

2.9 Biofilm inhibition assay

The development of biofilm on the surface of bacteria increases their pathogenicity and virulence and aids in developing bacterial resistance. Hence, bacteria are protected from antibiotic attack, reducing the bactericidal efficacy of antibacterial agents.[42,43] These biofilms promote bacterial absorption and reproduction on the surface of medical equipment, making it more difficult to use it clinically.[44] Using the crystal violet assay, we evaluated the ability of **ZnL_2** to suppress biofilm formation by *B. subtilis* and *S. enterica*. The inhibition of biofilm by active **ZnL_2** increases with the increase in concentration. **ZnL_2** was able to suppress the formation of biofilm of *B. subtilis* and *S. enterica* up to 24.3% and 30.2%, respectively, at the MIC value. As the concentration reached 8 × MIC, the complex inhibited biofilm formation by *B. subtilis* and *S. enterica* up to 75.2% and 87.1%, respectively (Fig. 4a). On the other hand, colistin inhibited the biofilm of *B. subtilis* and *S. enterica* 53.2% and 60.2%, respectively, at 8 × MIC (Fig. S9a). Comparing the biofilm inhibition ability of **ZnL_2** and colistin, the Zn complex displayed better biofilm inhibition properties than colistin towards both the tested strains. According to these findings, **ZnL_2** may prevent *B. subtilis* and *S. enterica* from forming biofilms, thus delaying the emergence of bacterial resistance. The same experiment was conducted in triplicate.

2.10 Biofilm virulence factor

2.10.1 Auto-aggregation. Bacterial adhesion to surfaces and self-aggregation promote the formation of biofilms, which act as protective barriers against antibiotics. This reduces drug penetration, lowers treatment effectiveness and contributes to the development of antimicrobial resistance.[45] Therefore, it is worthwhile to investigate the ability of the **ZnL_2** complex to reduce bacterial auto-aggregation. When *B. subtilis* and *S. enterica* were treated with **ZnL_2** as shown in Fig. 4b, the absorbance value of the supernatant at 600 nm increased gradually with the increasing concentration of the complex. On treating *B. subtilis* and *S. enterica* with colistin, the increase in the absorption value of the supernatant was less (Fig. S9b) as compared to **ZnL_2**, indicating that the **ZnL_2** complex has greater ability for self-auto aggregation in a concentration-dependent manner than colistin, thereby postponing the development of drug resistance. The same experiment was conducted in triplicate.

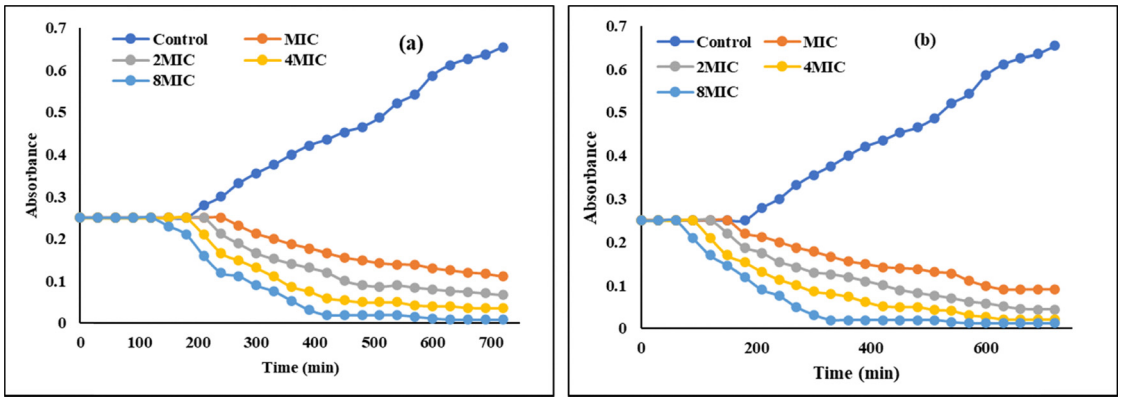

Fig. 3 Time–killing kinetics of (a) *B. subtilis* and (b) *S. enterica* treated with **ZnL_2** at various concentrations.

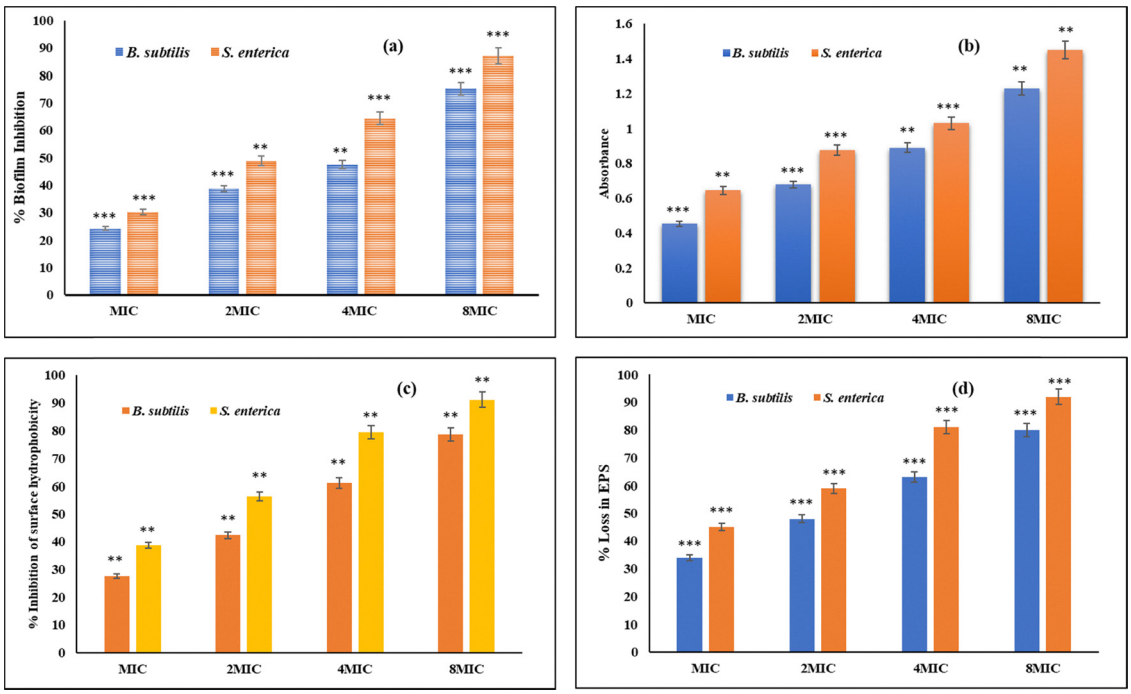

Fig. 4 (a) Inhibition of biofilm; (b) auto-aggregation; (c) inhibition of surface hydrophobicity; and (d) loss in the EPS content of *B. subtilis* and *S. enterica* in the presence of **ZnL_2**. *$P < 0.05$; **$P < 0.01$; ***$P < 0.001$. $n = 3$.

2.10.2 Surface hydrophobicity inhibition assay. The hydrophobicity of the cell surface, a critical virulence component that creates a robust biofilm, strengthens bacterial cell adhesion and subsequent colonization on the solid surface.[46] By using the microbial adhesion to hydrocarbon assay, it was possible to determine whether **ZnL_2** could reduce the hydrophobicity of *B. subtilis* and *S. enterica* surfaces. Interestingly, the complex **ZnL_2** significantly decreased the hydrophobicity of the tested bacterial strains. **ZnL_2** exhibited a concentration-dependent increase in suppressing the surface hydrophobicity of bacteria (Fig. 4c). At 8 × MIC concentration, **ZnL_2** reduced the hydrophobicity of *B. subtilis* and *S. enterica* by 78.6% and 91.2%, respectively. On the other hand, upon treating *B. subtilis* and *S. enterica with* colistin, the hydrophobicity reduced to 45.3% and 49.4%, respectively, at 8 × MIC (Fig. S9c). These findings suggested that **ZnL_2** could effectively decrease the hydrophobicity of both bacterial surfaces in comparison to colistin, thus preventing the biofilm virulence factor, which is the main cause of strong biofilm formation. The experiment was performed in triplicate.

2.10.3 Reduction in exopolysaccharides (EPS). The presence of EPS promotes the formation of a biofilm network and cell aggregation, which results in the emergence of drug resistance.[47] Therefore, a reduction in the content of exopolysaccharides was investigated to assess the potential of **ZnL_2** for preventing the formation of biofilms. The EPS content of *B. subtilis* and *S. enetrica* was observed to be decreased by 34.4% and 45.3% on treatment with **ZnL_2** at MIC concentration. The EPS content decreased more sharply as the concentration of **ZnL_2** increased, reaching 80.4% (*B. subtilis*) and 92.1% (*S. enterica*) at 8 × MIC, whereas the decrease in the EPS content of *B. subtilis* and *S. enterica* upon treating with colistin at 8 × MIC was found to be 64% and 74.3%, respectively (Fig. S9d). These results suggest that **ZnL_2** might successfully lower the exopolysaccharide content of both the tested bacteria in comparison to colistin, preventing biofilm formation and delaying the development of drug resistance, as shown in Fig. 4d. The same experiment was conducted in triplicate.

Combining the findings mentioned above, it is concluded that **ZnL_2** may successfully block the biofilm virulence factor that causes robust biofilm formation. It might also make it easier to break up the established biofilm, which would be beneficial for boosting the antibacterial activity and preventing the emergence of drug resistance.

2.11 Membrane disruption assay

By shielding the bacteria from external materials, their membranes perform a vital function in preserving the many metabolic events that occur in the right order.[48] The protective barrier constructed by bacterial membranes is the primary cause of decreased antibiotic permeability, which changes the concentration of medications that enter the bacteria and has a direct impact on their effectiveness and therapeutic values leading to the development of drug resistance.[49] Antibacterial agents are increasingly being developed with a focus on the cell membrane. We were motivated to investigate the potential of **ZnL_2** to disrupt the bacterial cell membrane further due to its excellent antibacterial efficacy, limited potential for drug resistance, and quick bactericidal properties.

2.11.1 Membrane depolarisation. By interfering with cells' transmembrane potential, the majority of drugs demonstrate

their bactericidal actions and cause cell death. Disc3,5-(dipropylthiadicarbocyanine), a potentiometric dye used to measure depolarisation, has been used to determine the capacity of ZnL_2 to depolarise the bacterial cell membrane.[50] The release of the dye from cells in the presence of ZnL_2 increases the intensity of fluorescence, a sign of membrane depolarization. Fig. 5 illustrates that the fluorescence intensity of the dye in *B. subtilis* and *S. enterica* rises gradually in a dose- and time-dependent manner after being incubated with ZnL_2, while untreated cells show no change. The increase in the fluorescence intensity of the dye in *B. subtilis* and *S. enterica* treated with colistin was less (Fig. S10a) as compared to that treated with ZnL_2. According to these findings, ZnL_2 was capable of effectively disrupting the membrane potential in comparison to colistin, thus retarding the rise of drug resistance.

2.11.2 Outer membrane permeability. Some antibiotics cannot penetrate the cell due to the protective barrier of a thick wall of peptidoglycan in *B. subtilis* and the outer membrane in *S. enterica*, which lowers their therapeutic values.[24] The disruption of the thick cell wall of *B. subtilis* and permeabilization of the outer membrane of *S. enterica*, incubated with ZnL_2, were evaluated using NPN (*N*-phenyl-1-naphthylamine), a fluorescent dye.[51] When NPN penetrates the damaged outer membrane and thick cell wall of bacteria, its fluorescence intensity increases; in contrast, when the cell membrane is intact, only weak fluorescence is observed. On treatment of *B. subtilis* and *S. enterica* with ZnL_2, the emission intensity increased gradually in both time-dependent and concentration-dependent modes, as shown in Fig. 6. The increase in the fluorescence intensity of *B. subtilis* and *S. enterica* treated with colistin was less (Fig. S10b) as compared to that treated with ZnL_2. These findings demonstrated that ZnL_2 might successfully damage the thick cell wall of *B. subtilis* and the outer membrane of *S. enterica*, hence postponing the emergence of antibiotic resistance.

2.11.3 Inner membrane permeability. An inner membrane experiment was performed using ethidium bromide (EtBr) to gain insight into the mechanism underlying the antibacterial activity of ZnL_2. Although EtBr is impermeable to intact cell membranes, but it readily enters bacteria with damaged membranes, where it binds to DNA and produce fluorescence.[52] A progressive increase in fluorescence intensity was seen after inoculating *B. subtilis* and *S. enterica* cells with ZnL_2 at a known concentration of EtBr, suggesting that there were more bacterial cells with damaged membranes in the inoculum. The concentration- and time-dependent increase in fluorescence intensity indicated that ZnL_2 can disrupt the inner membrane of both the tested bacterial strains (Fig. 7a–c). The increase in the fluorescence intensity of *B. subtilis* and *S. enterica* treated with colistin was less (Fig. S10c) as compared to that treated with ZnL_2.

B. subtilis and *S. enterica*, with or without ZnL_2, were stained with the EtBr dye and examined under a confocal laser scanning microscope to learn more about the antibacterial mechanism of the complex. When *B. subtilis* and *S. enterica* were treated with ZnL_2, a strong red fluorescence was seen, further suggesting that ZnL_2 could destroy *B. subtilis* and *S. enterica* cell membranes. In contrast, the control group in the absence of ZnL_2 showed no fluorescence, as illustrated in Fig. 7d and e.

Combining the findings mentioned above, it is proposed that ZnL_2 may efficiently harm the cell membrane of *B. subtilis* and *S. enterica* and induce membrane depolarisation, which in

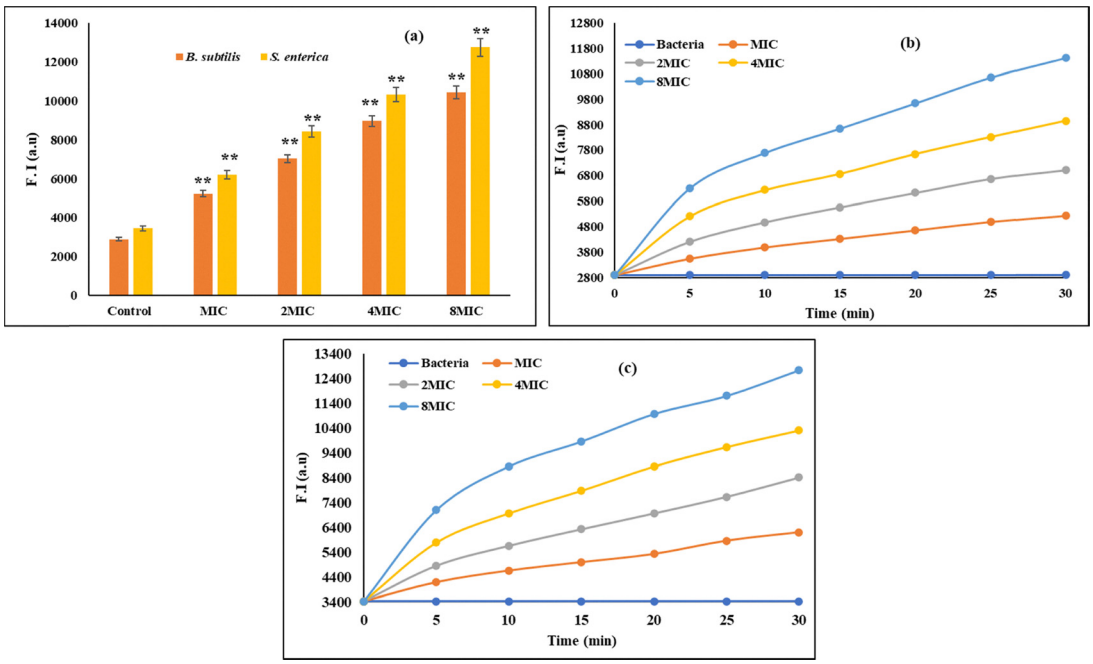

Fig. 5 Membrane depolarisation of *B. subtilis* and *S. enterica* by ZnL_2 (a) at different concentrations and in time-dependent mode against (b) *B. subtilis* and (c) *S. enterica*. *$P < 0.05$; **$P < 0.01$; ***$P < 0.001$. $n = 3$.

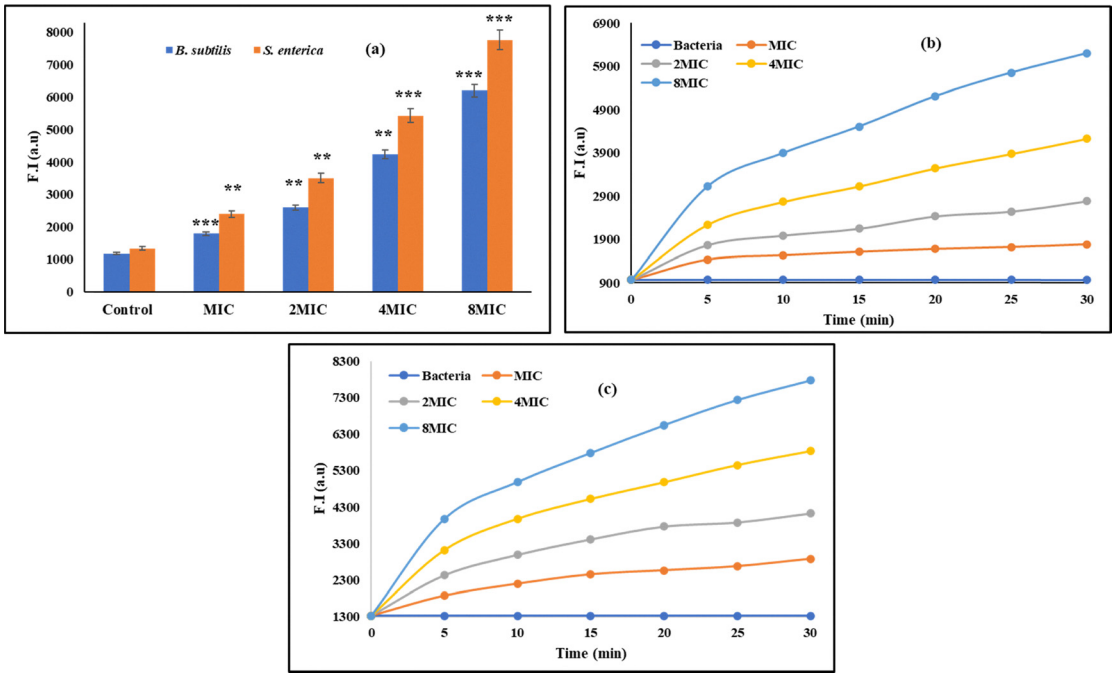

Fig. 6 Outer membrane permeability of *B. subtilis* and *S. enterica* by **ZnL_2** (a) at different concentrations and in time-dependent mode against (b) *B. subtilis* and (c) *S. enterica*. *$P < 0.05$; **$P < 0.01$; ***$P < 0.001$. $n = 3$.

turn may trigger cell apoptosis and, eventually, cell death, contributing to its antibacterial function. All the above experiments were performed in triplicate.

2.12 Leakage of cytoplasmic content

The integrity of their cell membranes maintains the stability and biological activity of bacteria; any damage to these membranes allows the cytoplasmic content, including protein and nucleic acids, to escape, leading to cell death.[53] Follin's test was employed to measure the amount of released protein from *B. subtilis* and *S. enterica* to verify the membrane damage caused by the **ZnL_2** complex. As the amount of **ZnL_2** increased, the concentration of leaked protein increased proportionately, as shown in Fig. 8a. As a result, the data showed conclusive evidence of membrane damage. Additionally, the concentrations of leaked nucleic acid from *B. subtilis* and *S. enterica* were measured to demonstrate the damage caused to the integrity of the membrane. **ZnL_2** exhibited a concentration-dependent increase in nucleic acid leaking from bacterial cells (Fig. 8b). The outcomes were consistent with membrane degradation. Both experiments were performed in triplicate.

2.13 Metabolic dysfunction

Bacterial metabolism sustains both the development and survival of microorganisms. Through a variety of metabolic processes, bacteria produce vital macromolecules, maintain cellular homeostasis, and obtain energy.[54] When cell membranes are disrupted, proteins on the surface become denatured, which results in metabolic dysfunction and ultimately cell death. The intracellular metabolic activity of *B. subtilis* and *S. enterica* in the presence of **ZnL_2** was assessed using the Almar blue test. After incubation with **ZnL_2**, the metabolic activity of *B. subtilis* and *S. enterica* dropped dramatically in a concentration-dependent manner (Fig. 9a). **ZnL_2** reduced the metabolic activity of *B. subtilis* and *S. enterica* by 25.4% and 19.6% at 8 × MIC, respectively, whereas in the presence of colistin, the metabolic activities of *B. subtilis* and *S. enterica* were reduced to 40.1% and 35.5%, respectively, at 8 × MIC (Fig. S11a). The result suggested that reduction in metabolic activity in the presence of **ZnL_2** was more as compared to colistin. The experiment was conducted in triplicate.

2.14 Intracellular oxidative stress

2.14.1 Reactive oxygen species (ROS). Under external stress, the ROS accumulation increases inside the bacterial cells, disrupting their cellular structure and resulting in oxidative stress. Many antibacterial agents show their activity by generating ROS inside the cells.[55,56] The ability of **ZnL_2** to cause oxidative stress in *B. subtilis* and *S. enterica* was assessed fluorometrically by measuring the amount of ROS in treated and untreated cells using the DCFH-DA fluorescent dye. The emission intensity of *B. subtilis* and *S. enterica* treated with **ZnL_2** increased in a concentration-dependent manner. The increase in the fluorescence intensity of *B. subtilis* and *S. enterica* treated with colistin was less (Fig. S11b) as compared to that treated with **ZnL_2**. Thus, **ZnL_2** can raise ROS levels, which can harm *B. subtilis* and *S. enterica* oxidatively and result in bacterial cell death (Fig. 9b).

2.14.2 Glutathione activity. Antioxidant glutathione (GSH), a tripeptide containing thiol, is present in normal bacterial cells in an excessive concentration in a reduced state, protects

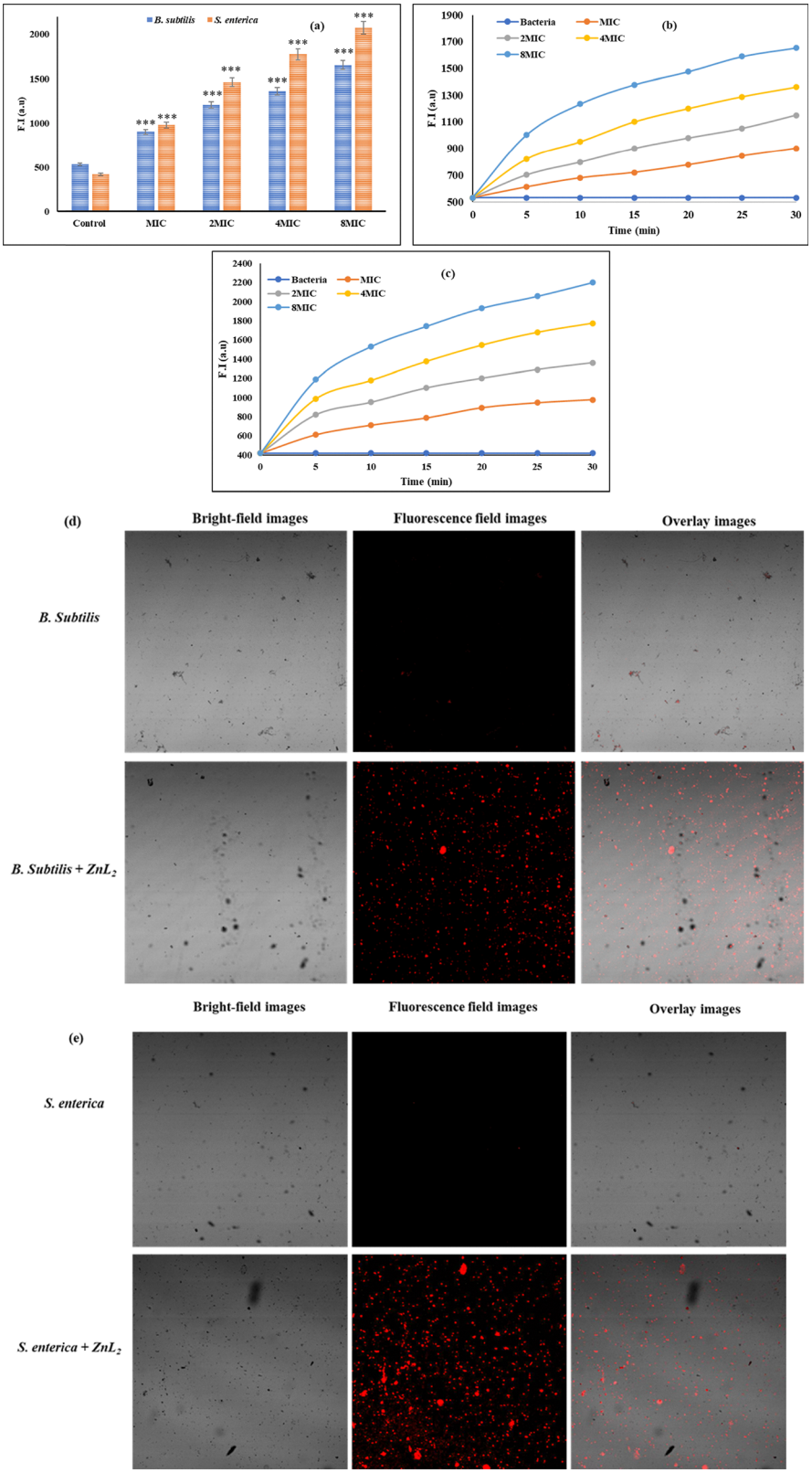

Fig. 7 Inner membrane permeability of *B. subtilis* and *S. enterica* by **ZnL_2** (a) at different concentrations and in time-dependent mode against (b) *B. subtilis* and (c) *S. enterica*; fluorescence micrographs stained with EtBr (d) control and after treatment of *B. subtilis* with **ZnL_2** at 1.56 μg mL^{-1}; (e) control and after treatment of *S. enterica* with **ZnL_2** at 1.56 μg mL^{-1}. $^{*}P < 0.05$; $^{**}P < 0.01$; $^{***}P < 0.001$. $n = 3$.

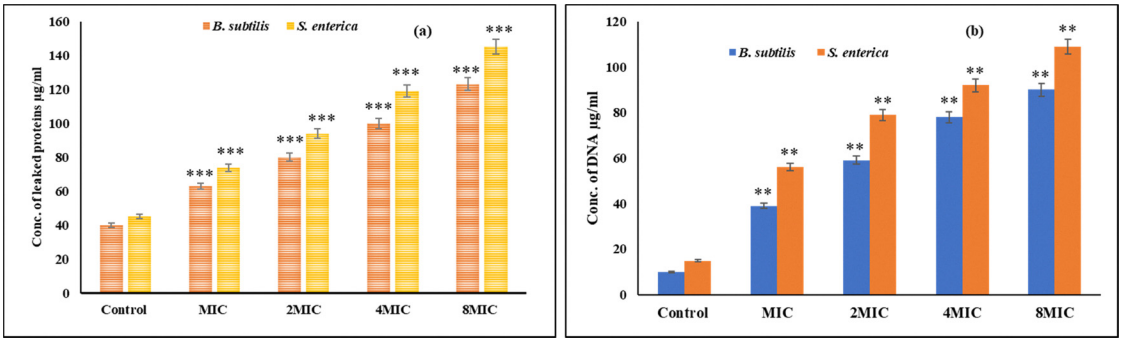

Fig. 8 (a) Protein leakage and (b) DNA leakage from *B. subtilis* and *S. enterica* in the presence of ZnL_2 at different concentrations.

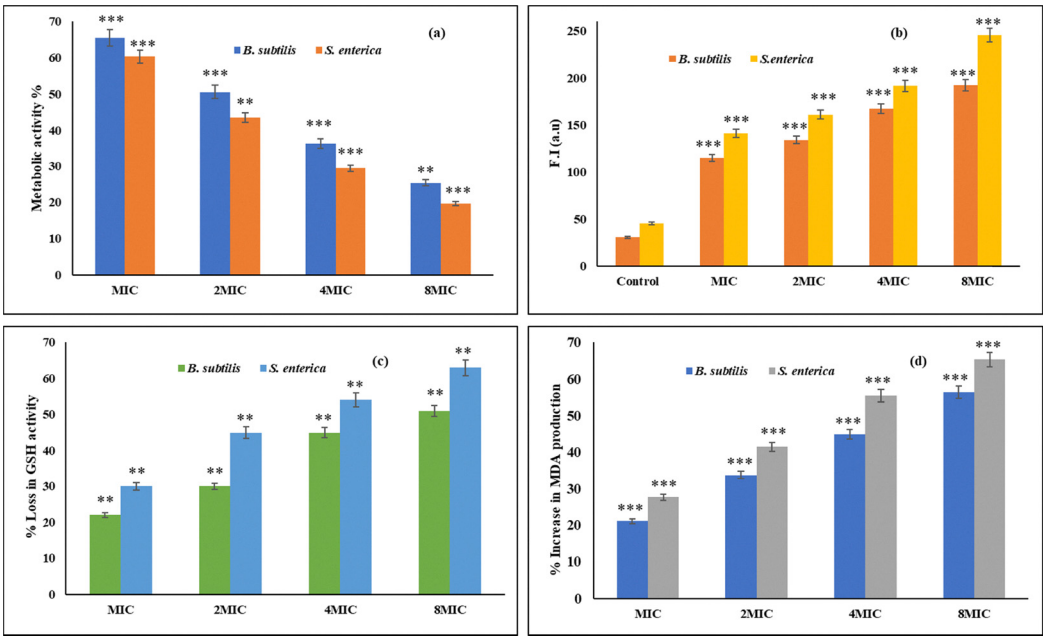

Fig. 9 (a) Loss in metabolic activity; (b) intracellular ROS production; (c) loss in GSH activity and (d) malondialdehyde production in *B. subtilis* and *S. enterica* treated with ZnL_2.

bacterial cells from damage caused due to oxidative stress, and preserves the ability of the cell to operate normally. An excess ROS level inside the cells makes it easier for GSH to change from its reduced to oxidized state, which renders GSH the ability to protect proteins, enzymes, DNA, and other materials from oxidative damage.[57] Elmann's method was employed to determine the decrease in GSH activity, which is a sign of oxidative stress generation. It was found that ZnL_2 might lower the amount of GSH in *B. subtilis* and *S. enterica*. When incubated with ZnL_2, the GSH levels of treated bacterial cells were decreased (Fig. 9c). The GSH level dropped in direct proportion to ZnL_2 concentration. At 8 × MIC, there was about 51% and 63% reduction in the GSH activity of *B. subtilis* and *S. enterica*, respectively, when treated with ZnL_2, whereas in the presence of colistin, the decrease in the GSH activity of *B. subtilis* and *S. enterica* was found to be 40% and 35.5%, respectively, at 8 × MIC (Fig. S11c). The result suggested that reduction in metabolic activity in the presence of ZnL_2 was more as compared to colistin. These findings provided more confirmation that the ZnL_2 complex produces ROS.

2.14.3 Lipid peroxidation. The formation of ROS within cells promotes lipid peroxidation in cells. The level of malondialdehyde (MDA) in cells represents the antioxidant capability and degree of oxidative damage to cells.[58] A metric used to assess the degree of lipid peroxidation is the rise in MDA levels within cells. ZnL_2 considerably increased the amount of MDA generated in *B. subtilis* and *S. enterica* (Fig. 9d). Furthermore, as ZnL_2 concentration increased, MDA generation progressively increased as well. MDA generation increased by 56.3% in the case of *B. subtilis* and by 65.3% in the case of *S. enterica*, when treated with ZnL_2 as the concentration reached 8 × MIC. These findings indicate that ZnL_2 promotes lipid peroxidation thereby contributing to bacterial cell death. The above experiments were performed in triplicate.

2.15 Change in the morphology of *B. subtilis and S. enterica* cells

The bacterial morphological modification using scanning electron microscopic (SEM) images further validated the damage caused to the *B. subtilis* and *S. enterica* membrane by $\mathbf{ZnL_2}$. Untreated *B. subtilis* and *S. enterica* cells exhibited regular, symmetrical, undamaged, and rod-shaped cells. Both the bacteria showed cell wall rupture and cytoplasmic content leakage after being treated with $\mathbf{ZnL_2}$ at 2 × MIC (Fig. 10). Furthermore, $\mathbf{ZnL_2}$ was discovered to cause *B. subtilis* and *S. enterica* cells to shrink and break. These findings verified that $\mathbf{ZnL_2}$ caused membrane damage in *B. subtilis* and *S. enterica*.

2.16 Interactions with DNA

Deoxyribonucleic acid (DNA), the storehouse of genetic information, is a frequently used molecular target for natural and synthetic drugs such as antitumor, antibacterial, and antiviral. Antibacterial drug development often targets bacterial DNA due to its critical role in cellular processes.[59] DNA encodes the genetic instructions for protein synthesis, which is fundamental for bacterial metabolism and function. Thus, exploring the binding affinity of DNA with $\mathbf{ZnL_2}$ with the help of absorption and emission spectroscopy can help us to build a potent antibacterial agent.

Fig. 11a displays the UV-visible absorption spectra of the zinc complex $\mathbf{ZnL_2}$ upon addition of ct-DNA in aq. HEPES buffer. The complex $\mathbf{ZnL_2}$ shows absorption peaks at 230 nm, 277 nm and 322 nm. On incremental addition of ct-DNA to the complex solution, the 230 nm and 277 nm peak show a hyperchromic shift, whereas the 322 nm peak shows hypochromic shift. In addition, a new peak around 365 nm was also observed on incremental addition of ct-DNA. ct-DNA binding with the ligand **L** was also performed to check the effectiveness in comparison with $\mathbf{ZnL_2}$ (Fig. S12). The binding constant for ligand **L** with ct-DNA was found to be $3.04 \times 10^5\ M^{-1}$ (Fig. S13). The binding constant for the interaction of $\mathbf{ZnL_2}$ with ct-DNA was found to be $4.05 \times 10^5\ M^{-1}$ (calculated using the Benesi–Hildebrand equation (Fig. S14)). A fluorescence titration by varying the concentration of ct-DNA in a solution of $\mathbf{ZnL_2}$ was also performed to understand the interaction between $\mathbf{ZnL_2}$ and ct-DNA (Fig. 11b). The zinc complex exhibits weak fluorescence (λ_{max} = 525 nm) (in HEPES buffer, pH 7.4) and on increasing the concentration of ct-DNA, the emission intensity of $\mathbf{ZnL_2}$ increases, which suggests the interaction between $\mathbf{ZnL_2}$ and ct-DNA (Fig. 11b). To assess the nature of complex's interaction with ct-DNA, a fluorescence titration was performed by incremental addition (0 to 75 μM) of the zinc complex to a 1 : 1 solution of ct-DNA and ethidium bromide (EtBr) (intercalating agent) in HEPES buffer (pH 7.4). The EtBr–DNA complex exhibited emission maxima at 601 nm (λ_{ex} = 480 nm) which decreased upon incremental addition of the zinc complex (Fig. 11c), due to the displacement of EtBr from the EtBr–DNA complex by the zinc complex. The results indicated that the complex binds to ct-DNA *via* an intercalative mode of interaction. The intercalation of $\mathbf{ZnL_2}$ into ct-DNA results in reduction of the available EtBr binding sites and further leads to a decrease in fluorescence intensity (Fig. 11c and Fig. S15). The reduction in fluorescence intensity indicates that $\mathbf{ZnL_2}$ binds to DNA and causes structural distortion at the tertiary or quaternary levels.

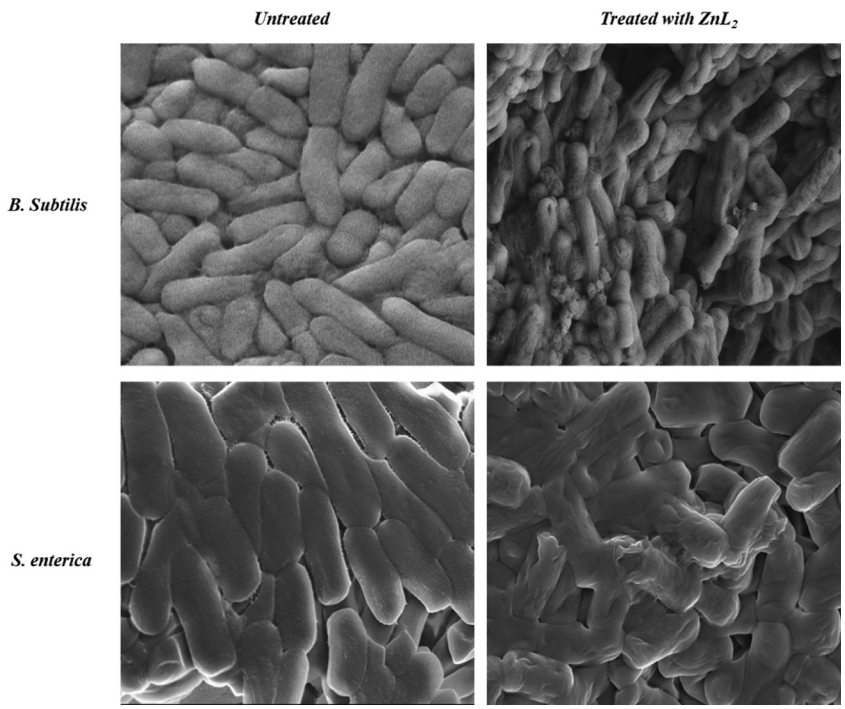

Fig. 10 SEM images of untreated and treated *B. subtilis* and *S. enterica* with $\mathbf{ZnL_2}$.

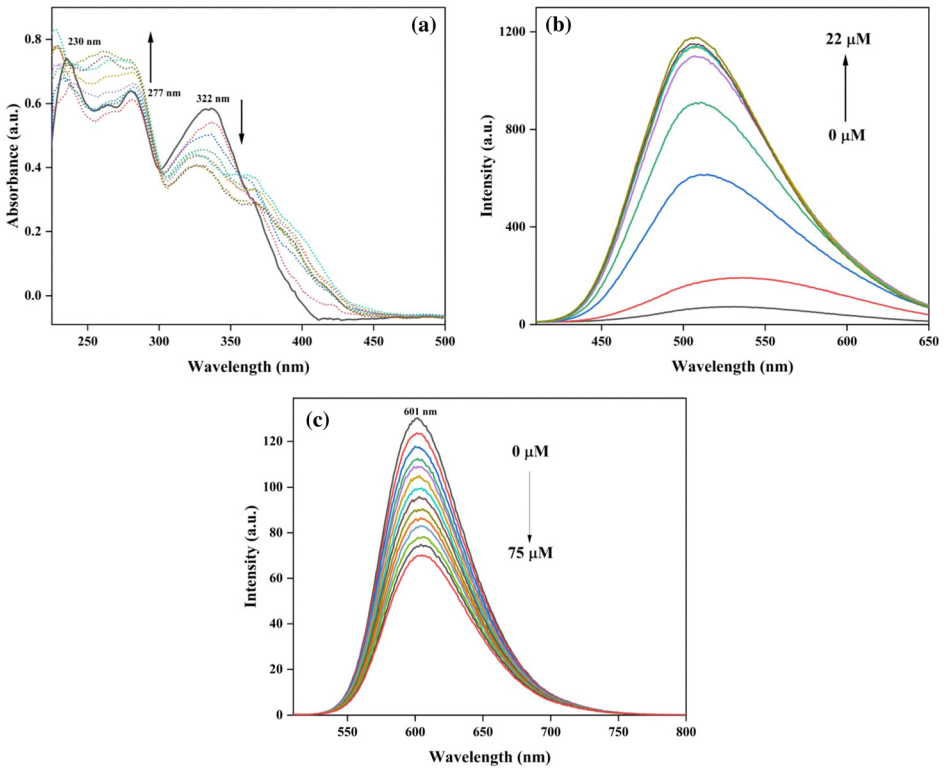

Fig. 11 (a) Absorption spectra and (b) emission spectra of **ZnL_2** with increasing concentration of ct-DNA in HEPES buffer (pH 7.4); (c) emission spectra of EtBr–ct-DNA in HEPES buffer with increasing concentration of **ZnL_2**.

2.17 HSA binding studies

The study of interaction of potential drugs with human serum albumin (HSA) is crucial for understanding various pharmacokinetic–pharmacodynamic properties, efficacy, and drug safety.[60] HSA is the most abundant protein in human plasma, and it plays a key role in the transportation and distribution of drugs throughout the body. The extent of binding can significantly affect the distribution of drugs in the body.[61] Highly bound drugs remain in the bloodstream longer, while those with low binding may diffuse more freely into tissues and organs. Spectroscopic techniques such as absorption and emission spectroscopy were employed to study the binding affinities of **ZnL_2** towards HSA.

The absorption spectrum of HSA (10 μM) in PBS buffer shows an absorption peak at 280 nm, which is attributed to aromatic amino acids like phenylalanine (Phen), tyrosine (Tyr), and tryptophan (Trp).[62] On gradual addition of **ZnL_2** (0–30 μM) to the HSA solution, a hyperchromic shift was observed at 280 nm along with a new peak at 332 nm (Fig. 12a). The absorption maxima of HSA at 280 nm remained unchanged even in the presence of **ZnL_2**, suggesting that **ZnL_2** binds with HSA through non-covalent interactions.[63] HSA binding with the

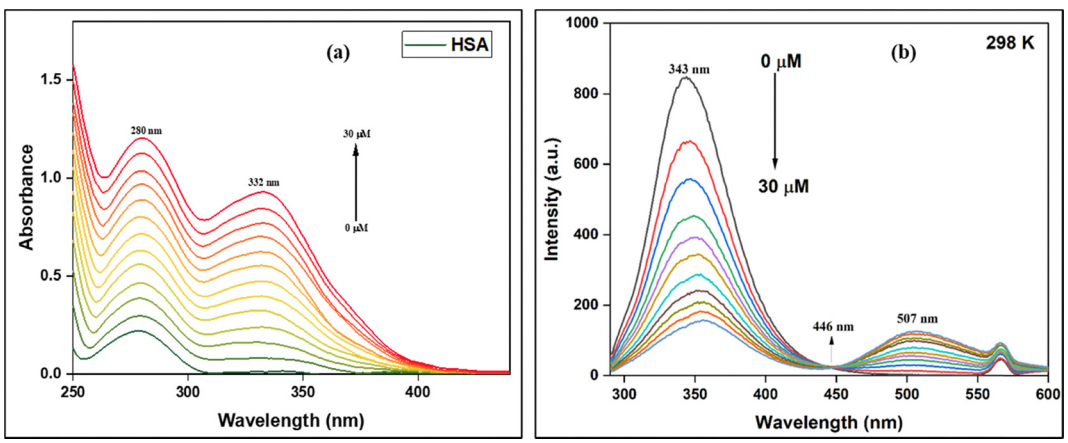

Fig. 12 (a) Absorption and (b) emission spectra of HSA with increasing concentration of **ZnL_2** at 298 K in PBS buffer (pH 7.4).

ligand **L** was also performed to compare the efficiency with that of $\mathbf{ZnL_2}$ (Fig. S16 and S17). The binding constant (K_b) was determined by the Benesi–Hildebrand plot (Fig. S18) and was found to be 0.87×10^6 M^{-1}.

A fluorescence titration experiment was further carried out to study the mode of interaction between the complex and ligand with HSA (Fig. S19–S23). Upon excitation at 280 nm, the free HSA (10 μM) solution in phosphate buffer (pH = 7.4) showed an intrinsic fluorescent band at 350 nm because of the amino acid residues Tyr, Trp, and Phe. The fluorescence intensity of HSA at 350 nm was decreased gradually after the addition of $\mathbf{ZnL_2}$ (0–30 μM) to the solution of HSA (10 μM) in phosphate buffer (Fig. 12b). An isosbestic point was observed at 446 nm, representing the equilibrium between HSA and $\mathbf{ZnL_2}$ and the rise of a new peak at 507 nm. A slight red shift of 10 nm deviation at 343 nm was observed when the concentration of the complex was increased, which can be speculated due to the increase in the polarity of the microenvironment around the tryptophan residue. The emission intensity of HSA was suppressed entirely at increasing $\mathbf{ZnL_2}$ complex concentrations, demonstrating the effective binding of $\mathbf{ZnL_2}$ with HSA. When HSA interacts with a foreign ligand, the microenvironment changes, which causes quenching of the fluorescence intensity. The Stern–Volmer equation was utilised to determine the quenching mechanism. The quenching constant (K_{sv}) and the bimolecular quenching constant (K_q) (Fig. S22 and S23) were analysed and found to be 1.71×10^5 M^{-1} and 1.71×10^{13} M^{-1}, respectively. As K_q is greater than the maximum value for dynamic quenching of biopolymers (2×10^{10} M^{-1} s^{-1}), a ground-state complex is likely to be formed from the association of the compound with HSA, attributing to the static quenching mechanism. Furthermore, by calculating the binding constant values, the stability of complexes for the interaction of $\mathbf{ZnL_2}$ with HSA was evaluated. The binding constant parameters were thus determined using the modified Stern–Volmer equation and found to be 1.46×10^6 M^{-1} (K_b), indicating the effective binding of $\mathbf{ZnL_2}$ with HSA (Fig. S23). The binding stoichiometry was determined to be approximately 1, indicating that $\mathbf{ZnL_2}$ binds with HSA at a single site with 1 : 1 stoichiometry. Furthermore, Gibb's free energy was determined and found to be −8.38 kcal mol^{-1}. The spontaneous binding process between $\mathbf{ZnL_2}$ and HSA was predicted by this negative value of ΔG, which suggested that hydrogen bonds and van der Waals interactions are in charge of the binding between $\mathbf{ZnL_2}$ and HSA. By consolidating the results from various studies, it was concluded that $\mathbf{ZnL_2}$ binds effectively to HSA, facilitating its efficient transport to the target site for combating bacterial infections.

Table 3 Binding constants K_b of $\mathbf{ZnL_2}$ HSA–probe systems at 298 K in the absence and presence of site markers

$\mathbf{ZnL_2}$	K_b (10^6 L mol^{-1})	n
Blank	1.46	1.00
Warfarin	1.40	1.21
Ibuprofen	0.54	1.10

To determine the binding site of $\mathbf{ZnL_2}$ towards HSA, we performed the drug displacement studies with ibuprofen and warfarin as site markers. With incremental additions of $\mathbf{ZnL_2}$, the emission bands of complexes of HSA–warfarin and HSA–ibuprofen at 350 nm were quenched (Fig. 13). From the modified Stern–Volmer equation, the binding constant (K_b) for $\mathbf{ZnL_2}$–HSA in the presence of warfarin was found to be 1.46×10^6 L mol^{-1} (Fig. S24). In contrast, in the presence of drug ibuprofen, the binding constant for $\mathbf{ZnL_2}$–HSA was found to be 0.54×10^6 L mol^{-1} (Fig. S25) (Table 3). It has been observed that the binding constant of $\mathbf{ZnL_2}$ has been significantly decreased in the presence of site marker ibuprofen. These results demonstrated that ibuprofen prevents the binding of $\mathbf{ZnL_2}$, suggesting that $\mathbf{ZnL_2}$ binds to HSA Suldow's site II.

Time-resolved emission studies were also conducted to determine the quenching mechanism responsible for the interaction of $\mathbf{ZnL_2}$ with HSA. According to steady-state emission studies, the binding interactions between HSA and $\mathbf{ZnL_2}$ are caused by static quenching. Time-resolved spectra of native HSA (10 μM) with and without the progressive addition of $\mathbf{ZnL_2}$ (0–30 μM) were recorded (Fig. S26). On addition of $\mathbf{ZnL_2}$, the native HSA's time decay profile decreased, suggesting the

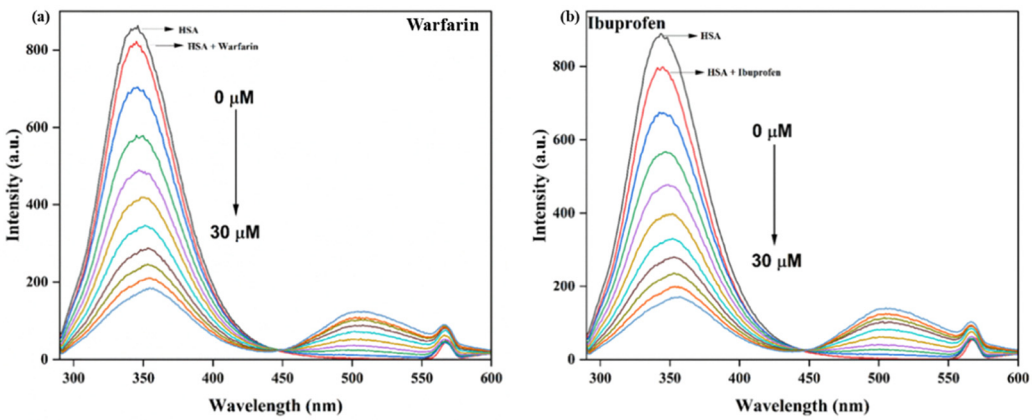

Fig. 13 Effect of $\mathbf{ZnL_2}$ on the emission spectra of the (a) warfarin–HSA complex and (b) ibuprofen–HSA complex.

Table 4 Lifetime fluorescence decay of HSA on interaction with **ZnL_2**

System	Conc.	τ_1 [ns]	τ_2 [ns]	τ_3 [ns]	α_1	α_2	α_3	*T*av	$\chi 2$
HSA		2.58	7.16	0.91	0.21	0.65	0.14	5.32	1.05
HSA-**ZnL_2**	01 : 01	1.99	6.39	0.40	0.12	0.10	0.78	1.17	1.08
	01 : 02	1.83	6.95	0.21	0.09	0.04	0.86	0.65	1.03
	01 : 03	1.44	6.20	0.08	0.04	0.02	0.95	0.24	1.07

presence of dynamic quenching (Table 4). Combining the findings from time-resolved and steady-state fluorescence investigations, it is proposed that **ZnL_2** interacts with HSA through both static and dynamic quenchings.[64]

3. Conclusion

As the threat of multidrug-resistant bacteria rises, the demand for new antibacterial drugs has become critical, but developing a drug with minimal resistance risk remains a considerable challenge. To address this issue, we have developed a zinc complex with 4′-(3,4-diethoxyphenyl)-2,2′:6′,2″-terpyridine (**L**) in 1 : 2 ratio (**ZnL_2**) as a promising antibacterial agent to tackle severe drug resistance. The synthesized **ZnL_2** was characterized by NMR, HRMS, FTIR, and SC-XRD studies. Initial bioactivity tests and structure–activity relationship analysis revealed that **ZnL_2** exhibited remarkable effectiveness in inhibiting bacterial growth. The complex showed excellent antibacterial activity against most of the tested bacterial strains with low MIC values ranging from 6.25 μg mL^{-1} to 1.56 μg mL^{-1} and outperformed the marketed drugs. **ZnL_2** significantly inhibited the biofilm formation, leading to a delay in the emergence of drug resistance. The complex **ZnL_2** effectively disrupts the bacterial membrane, reduces metabolic activity, and disrupts the biofilm virulence factor responsible for forming a strong biofilm, thus causing leakage of intercellular protein and nucleic acid contents. Additionally, bio-functional analysis reveals that **ZnL_2** can generate ROS within cells, which can lead to oxidative stress accumulation and GSH oxidation to GSSG, which in turn causes a decrease in GSH activity and oxidative cell damage. **ZnL_2** can easily transport to the target region and has good antibacterial activity because it may bind with DNA and HSA to form supramolecular complexes. Superior efficacy against bacterial strains, membrane disruption, drug-likeness, biofilm inhibition, oxidative stress damage, and metabolic dysfunction were all demonstrated by **ZnL_2** in comparison to marketed drugs. The complex **ZnL_2** can effectively overcome drug resistance and can be taken further for clinical trials for its development as a potent antibacterial agent.

4. Experimental section

4.1 Chemistry

The chemicals used for synthesis were purchased from SRL and Sigma Aldrich and used without any further purification. Ligand **L** was synthesised according to the reported method[29] and the synthetic procedure mentioned in the SI. The ^{1}H NMR spectrum was recorded on a 400 MHz Bruker NMR spectrometer to characterise the compounds. High resolution mass spectrometry (HRMS) of the synthesized analogues was performed using the Agilent 6545XT Advance Bio LC/Q-TOF. The FT-IR spectrum was recorded with a Bruker Hyperion 3000 FT-IR spectrometer. A Biotek ELISA plate was used for conducting bacterial studies. All the absorption studies were conducted on a Shimadzu UV-visible spectrophotometer. A HITACHI-F4600 fluorescence spectrophotometer was used for emission studies, and SEM was performed on a Carl Zeiss Sigma 500 FEG-SEM.

4.2 Synthesis of 1 : 2 Zinc complex ZnL_2

A methanolic solution of ligand **L** (0.2 mmol, 79.6 mg) and zinc nitrate hexahydrate (0.1 mmol, 29.7 mg) was heated at 60 °C and stirred for 2 h at room temperature. Further, sodium perchlorate solution (0.1 mmol, 12.20 mg) was added to it and stirred for another 2 h to obtain yellow precipitates. The precipitates were filtered, followed by washing with ethanol and distilled water. Slow diffusion of di-isopropyl ether into an acetonitrile–methanol (1 : 1) solution of **ZnL_2** gave yellow-coloured crystals. Yield (85%). HRMS $[C_{50}H_{46}N_6O_4Zn + ClO_4]^+$ *m*/*z* 959.2336 (calcd. 959.7820); ^{1}H NMR (400 MHz, DMSO-d_6) δ/ppm 9.26 (s, 4H), 9.14–9.12 (d, 4H), 8.30–8.26 (t, 4H), 8.03–8.01 (d, 2H), 7.95–7.90 (m, 6H), 7.52–7.48 (t, 4H), 7.32–7.30 (d, 2H), 4.35–4.30 (q, 4H), 4.25–4.20 (q, 4H), 1.47–1.41 (dt, 12H). FT-IR (υ_{max}/cm^{-1}): 3593(H_2O), 3093 (aromatic sp^2-C–H str), 2982 (sp^3-C–H asym str of –CH_3), 2931 (sp^3-C–H asym str of –CH_2), 2874 (sp^3-C–H sym str of –CH_3), 1602, 1523, 1474, 1434 (aromatic C═C, C═N str), 1407, 1257 (aromatic C–O asym str), 1206, 1153 (aliphatic C–O str), 1081 (aromatic C–O sym str), 859 (C–H bending, *p*-sub), 791 (C–H bending, *m*-sub), 689 (C–H bending, *m*-sub), 622.

4.3 Quantum chemical studies

The 3D structures of ligand **L** and **ZnL_2** were built in the GaussView. The Gaussian 16W suite of programs was used to execute theoretical calculations of the ligand **L** and **ZnL_2**, and these were optimized with DFT calculations using the B3LYP level of the 6–311++G(d,p) basis set for C, O, N, and H, whereas the LANL2DZ basis set was used for zinc atoms with no symmetry constraints in the gas phase. The frontier molecular orbitals, namely the highest occupied molecular orbital (HOMO) and the lowest unoccupied molecular orbital (LUMO), were generated using the cubegen module and visualized with Chemcraft software. These orbital plots were used to qualitatively examine the electronic distribution and nature of frontier orbitals, providing supportive insight into the electronic characteristics of ligand L and the **ZnL_2** complex.

Author contributions

S.S.: synthesis, characterisation, and methodology; S. G.: conceptualization, methodology, and drafting; P.S.: data curation; D.D.: data curation; K. P.: visualization, investigation,

supervision and editing; B.N.G.: conceptualization, investigation, supervision and editing.

Conflicts of interest

The authors declare no competing financial interest.

Data availability

Data shall be available on request.

Supplementary information (SI) is available. Supporting information: materials and methods; crystallographic data (CCDC 2424188); additional tables and figures of related biological studies; spectral and other characterization data for key target compounds. A separate.zip folder containing the raw data images for Fig. 7(d) and (e) is provided – the software used for image analysis is FV-10 ASW 4.2 Viewer. See DOI: https://doi.org/10.1039/d5ma00502g.

CCDC 2424188 contains the supplementary crystallographic data for this paper.[65]

Acknowledgements

The authors acknowledge IIT Patna for providing the NMR data and NIT Rourkela for the HRMS data. The authors also acknowledge DST and SC-XRD Lab, SAIF-IIT Madras and crystallographer Dr Shobhana Krishnaswamy for data collection, structure solution and refinement. The authors S.S., P.S. and D.D. extend their gratitude to NIT Silchar for the Institute Fellowship and the facilities provided. K.P. thanks the SERB, New Delhi (CRG/2023/004080), and CEEMS (Project No: TIET/CEEMS/Regular/2021/018), VT-India, for providing funds.

References

1 A. Kumar, A. K. Singh, H. Singh, V. Vijayan, D. Kumar, J. Naik, S. Thareja, J. P. Yadav, P. Pathak and M. Grishina, Nitrogen Containing Heterocycles as Anticancer Agents: A Medicinal Chemistry Perspective, *Pharmaceuticals*, 2023, **16**(2), 299.

2 J. Hu, W. Wu and C. Yang, Recent Advances in the Synthesis and Applications of Nitrogen-Containing Macrocyclic Arenes, *Molecules*, 2025, **30**(17), 3646.

3 P. V. Ledade, T. L. Lambat, J. K. Gunjate, P. K. P. G. Chopra, A. V. Bhute, M. R. Lanjewar, P. M. Kadu, U. J. Dongre and S. H. Mahmood, Nitrogen-Containing Fused Heterocycles: Organic Synthesis and Applications as Potential Anticancer Agents, *Curr. Org. Chem.*, 2023, **27**(3), 206–222.

4 R. Ranjith, The Chemistry and Biological Significance of Imidazole, Benzimidazole, Benzoxazole, Tetrazole and Quinazolinone Nucleus, *J. Chem. Pharm. Res.*, 2016, **8**(5), 505–526.

5 R. Pal, G. S. P. Matada, G. Teli, M. Saha and R. Patel, Therapeutic Potential of Anticancer Activity of Nitrogen-Containing Heterocyclic Scaffolds as Janus Kinase (JAK) Inhibitor: Biological Activity, Selectivity, and Structure–Activity Relationship, *Bioorg. Chem.*, 2024, 107696.

6 R. Musiol, P. Malecki, M. Pacholczyk and J. Mularski, Terpyridines as Promising Antitumor Agents: An Overview of Their Discovery and Development, *Expert Opin. Drug Discovery*, 2022, **17**(3), 259–271.

7 K. Velugula, A. Kumar and J. P. Chinta, Nuclease and Anticancer Activity of Antioxidant Conjugated Terpyridine Metal Complexes, *Inorg. Chim. Acta*, 2020, **507**, 119596.

8 S. Behera, P. P. Dash, A. K. Bishoyi, K. Dash, P. Mohanty, C. R. Sahoo, R. N. Padhy, M. Mishra, B. N. Ghosh and H. Sahoo, Protein Interactions, Molecular Docking, Antimicrobial and Antifungal Studies of Terpyridine Ligands, *J. Biomol. Struct. Dyn.*, 2023, **41**(20), 11274–11285.

9 D. Chao and Y. Zhang, Aggregation Enhanced Luminescent Detection of Homocysteine in Water with Terpyridine-Based Cu2+ Complexes, *Sens. Actuators, B*, 2017, **245**, 146–155.

10 K. Velugula and J. P. Chinta, Silver Nanoparticles Ensemble with Zn(II) Complex of Terpyridine as a Highly Sensitive Colorimetric Assay for the Detection of Arginine, *Biosens. Bioelectron.*, 2017, **87**(Ii), 271–277.

11 S. F. Kainat, M. B. Hawsawi, E. U. Mughal, N. Naeem, A. M. Almohyawi, H. M. Altass, E. M. Hussein, A. Sadiq, Z. Moussa and A. S. Abd-El-Aziz, Recent Developments in the Synthesis and Applications of Terpyridine-Based Metal Complexes: A Systematic Review, *RSC Adv.*, 2024, **14**(30), 21464–21537.

12 D. Das, S. Sutradhar, K. Rissanen and B. N. Ghosh, Synthesis and Structure of Trimethylplatinum(IV) Iodide Complex of 4′-(4-Methoxyphenyl)-2,2′:6′,2″-Terpyridine Ligand and Its Halogen Bonding Property, *Z. Anorg. Allg. Chem.*, 2020, **646**(5), 301–306.

13 B. N. Ghosh, M. Lahtinen, E. Kalenius, P. Mal and K. Rissanen, 2, 2′: 6′, 2 ″-Terpyridine Trimethylplatinum (Iv) Iodide Complexes as Bifunctional Halogen Bond Acceptors, *Cryst. Growth Des.*, 2016, **16**(5), 2527–2534.

14 S. Sutradhar, D. Das and B. N. Ghosh, Copper(II) and Cadmium(II) Triggered Hydrogelation of a Simple Trimethoxy Terpyridine Ligand, *J. Mol. Struct.*, 2022, **1265**, 133442.

15 S. Sutradhar, S. Basak, D. Das and B. N. Ghosh, Hydrogelation Behaviour of Methoxy Terpyridine Ligand Induced by Transition Metal Ions, *Polyhedron*, 2023, **236**, 116344.

16 S. Sutradhar, G. K. Suresh, S. Sarma, D. Das, P. Sarkar, S. G. Patra and B. N. Ghosh, Sulphide and Iodide Anion Recognition by a Selective Copper Hydrogel of a Chloro Substituted Terpyridine Ligand, *Inorg. Chem. Commun.*, 2024, **170**, 113263.

17 S. Sutradhar, S. Sarma, S. Palo, P. Sarkar, T. K. Sarma and B. N. Ghosh, Copper-Induced Tert-Butoxy-Substituted Terpyridine Hydrogel for Enhanced Peroxidase-like Activity and Colourimetric Glutathione Sensing, *New J. Chem.*, 2025, **49**(38), 16713–16722.

18 E. Athanasopoulos and J. Conradie, DFT Study of the Spectroscopic Behaviour of Different Iron(II)-Terpyridine Derivatives with Application in DSSCs, *J. Mol. Graphics Modell.*, 2024, **129**, 108753.

19 D. El-Sherbiny, H. Cheema, F. El-Essawy, A. Abdel-Megied and A. El-Shafei, Synthesis and Characterization of Novel Carbazole-Based Terpyridyl Photosensitizers for Dye-Sensitized Solar Cells (DSSCs), *Dyes Pigm.*, 2015, **115**, 81–87.
20 F. S. Al-Fartusie and S. N. Mohssan, Essential Trace Elements and Their Vital Roles in Human Body. *Indian J Adv, Chem. Sci.*, 2017, **5**(3), 127–136.
21 G. Bahr; P. E. Tomatis and A. J. Vila, *The Biochemistry and Enzymology of Zinc Enzymes*, 2023.
22 M. Porchia, M. Pellei, F. Del Bello and C. Santini, Zinc Complexes with Nitrogen Donor Ligands as Anticancer Agents, *Molecules*, 2020, **25**(24), 5814.
23 S. Nasiri Sovari and F. Zobi, Recent Studies on the Antimicrobial Activity of Transition Metal Complexes of Groups 6–12, *Chemistry*, 2020, **2**(2), 418–452.
24 J.-S. Zhao, N. Ahmad, S. Li and C.-H. Zhou, Hydrazyl Hydroxycoumarins as New Potential Conquerors towards Pseudomonas Aeruginosa, *Bioorg. Med. Chem. Lett.*, 2024, **103**, 129709.
25 G. Muteeb, M. T. Rehman, M. Shahwan and M. Aatif, Origin of Antibiotics and Antibiotic Resistance, and Their Impacts on Drug Development: A Narrative Review, *Pharmaceuticals*, 2023, **16**(11), 1615.
26 I. Tsonis, L. Karamani, P. Xaplanteri, F. Kolonitsiou, P. Zampakis, G. Gatzounis, M. Marangos and S. F. Assimakopoulos, Spontaneous Cerebral Abscess Due to Bacillus Subtilis in an Immunocompetent Male Patient: A Case Report and Review of Literature, *World J. Clin. Cases*, 2018, **6**(16), 1169.
27 S. M. Jajere, A Review of Salmonella Enterica with Particular Focus on the Pathogenicity and Virulence Factors, Host Specificity and Antimicrobial Resistance Including Multidrug Resistance, *Vet. world*, 2019, **12**(4), 504.
28 A. K. Bhunia and A. K. Bhunia, Salmonella Enterica, in *Foodborne Microbial Pathogens: Mechanisms and Pathogenesis*, 2018, pp. 271–287.
29 D. Das, S. Sutradhar, A. Singh and B. N. Ghosh, Zinc-Terpyridine Based Chemosensor for Detection of Pyrophosphate Anion in Aqueous Medium, *Z. Anorg. Allg. Chem.*, 2021, **647**(11), 1234–1238.
30 B. N. Ghosh, F. Topić, P. K. Sahoo, P. Mal, J. Linnera, E. Kalenius, H. M. Tuononen and K. Rissanen, Synthesis, Structure and Photophysical Properties of a Highly Luminescent Terpyridine-Diphenylacetylene Hybrid Fluorophore and Its Metal Complexes, *Dalton Trans.*, 2015, **44**(1), 254–267.
31 B. N. Ghosh, R. Puttreddy and K. Rissanen, Synthesis and Structural Characterization of New Transition Metal Complexes of a Highly Luminescent Amino-Terpyridine Ligand, *Polyhedron*, 2020, **177**, 114304.
32 Y.-M. Tan, J. Zhang, Y.-J. Wei, Y.-G. Hu, S.-R. Li, S.-L. Zhang and C.-H. Zhou, Cyanomethylquinolones as a New Class of Potential Multitargeting Broad-Spectrum Antibacterial Agents, *J. Med. Chem.*, 2024, **67**(11), 9028–9053.
33 T. J. Harrison, X. Chen, K. Yasoshima and D. Bauer, Phototoxicity—Medicinal Chemistry Strategies for Risk Mitigation in Drug Discovery, *J. Med. Chem.*, 2023, **66**(14), 9345–9362.
34 H. Sun, M. F. Ansari, N. Battini, R. R. Y. Bheemanaboina and C.-H. Zhou, Novel Potential Artificial MRSA DNA Intercalators: Synthesis and Biological Evaluation of Berberine-Derived Thiazolidinediones, *Org. Chem. Front.*, 2019, **6**(3), 319–334.
35 S.-F. Cui, D. Addla and C.-H. Zhou, Novel 3-Aminothiazolquinolones: Design, Synthesis, Bioactive Evaluation, SARs, and Preliminary Antibacterial Mechanism, *J. Med. Chem.*, 2016, **59**(10), 4488–4510.
36 Y.-G. Hu, N. Battini, B. Fang and C.-H. Zhou, Discovery of Indolylacryloyl-Derived Oxacins as Novel Potential Broad-Spectrum Antibacterial Candidates, *Eur. J. Med. Chem.*, 2024, **270**, 116392.
37 H. Huo, W. Dan, L. Qin, J. Bo, X. Zhang, C. Yang, B. Bai, J. Ren, B. Shi and J. Li, Novel Steroidal β-Carboline Derivatives as Promising Antibacterial Candidates against Methicillin-Resistant Staphylococcus Aureus, *Eur. J. Med. Chem.*, 2025, **283**, 117187.
38 H. Huo, W. Dan, M. Li, Y. Chen, C. Yang, L. Wu, B. Shi and J. Li, Design, Synthesis, and Biological Evaluation of Steroidal Indole Derivatives as Membrane-Targeting Antibacterial Candidates, *Eur. J. Med. Chem.*, 2025, **283**, 117156.
39 S. Rani and K. Paul, Triphenylethylene Analogues: Design, Synthesis and Evaluation of Antitumor Activity and Topoisomerase Inhibitors, *Eur. J. Med. Chem.*, 2020, **208**, 112775.
40 M. Shakir, A. Ali, S. Lakshmi, M. Garg, H. T. A. Almuqdadi, I. Irfan, M. Kamthan, M. C. Joshi, S. Javed and D. S. Rawat, Synthesis and Mechanistic Studies of 4-Aminoquinoline-Isatin Molecular Hybrids and Schiff's Bases as Promising Antimicrobial Agents, *Eur. J. Med. Chem.*, 2025, **283**, 117127.
41 Y. Yi, J. Zhang, S. Lin, H. Wang, G. Li, S. Yang, R. Shang, R. Zhang and F. Li, Design, Synthesis, and Biological Evaluation of Novel Pleuromutilin Derivatives with Methicillin-Resistant Staphylococcus Aureus-Targeting Phenol Linker Groups, *Eur. J. Med. Chem.*, 2025, **282**, 117061.
42 W. Guo, Z. Yang, K. Wang, W. Li, Y. Zhao, Y. Yang, W. Chang, Z. Gong, Z. Liu and Y. Chen, Discovery of Unique Bis-Substituted Aromatic Amide Derivatives as Novel Highly Potent Antibiotics for Combating Methicillin-Resistant Staphylococcus Aureus (MRSA), *J. Med. Chem.*, 2024, **67**(3), 2129–2151.
43 A. Vishwakarma; F. Dang; A. Ferrell; H. A. Barton and A. Joy, *Peptidomimetic Polyurethanes Disrupt Surface Established Bacterial Biofilms and Prevent Biofilm Formation*, 2021.
44 S. Guo, Q. Huang, Y. Chen, J. Wei, J. Zheng, L. Wang, Y. Wang and R. Wang, Synthesis and Bioactivity of Guanidinium-Functionalized Pillar [5] Arene as a Biofilm Disruptor, *Angew. Chem., Int. Ed.*, 2021, **60**(2), 618–623.
45 Q.-W. Lin, J.-Q. Lu, Y.-S. Huang, J.-J. Liu, W.-M. Chen and J. Lin, Cyclic Diguanylate G-Quadruplex Inducer-Nitric Oxide Donor Conjugate as a Bifunctional Antibiofilm Agent and Antibacterial Synergist against Pseudomonas Aeruginosa with a Hyperbiofilm Phenotype, *J. Med. Chem.*, 2023, **66**(17), 11927–11939.
46 O. Ciofu, C. Moser, P. Ø. Jensen and N. Høiby, Tolerance and Resistance of Microbial Biofilms, *Nat. Rev. Microbiol.*, 2022, **20**(10), 621–635.

47 J. Zhang, C. Chen, J. Chen, S. Zhou, Y. Zhao, M. Xu and H. Xu, Dual Mode of Anti-Biofilm Action of G3 against Streptococcus Mutans, *ACS Appl. Mater. Interfaces*, 2020, **12**(25), 27866–27875.

48 S. Gupta and K. Paul, Membrane-Active Substituted Triazines as Antibacterial Agents against Staphylococcus Aureus with Potential for Low Drug Resistance and Broad Activity, *Eur. J. Med. Chem.*, 2023, **258**, 115551.

49 S. He, X. Li, Y. Wei, L. Zhang, J. Wang, Z. Yang and A. Shan, Cuminaldehyde Potentiates Antiproteolytic Peptide Efficacy via Parallel Pathways of Enhanced Inner Membrane-Damaging Activity and Inhibition of Bacterial Energy Metabolism, *J. Med. Chem.*, 2024, **68**(1), 776–791.

50 S. Akhtar, M. M. Ansari, R. D. Verma, J. Sharma, A. Gupta, R. K. Dhuriya, D. P. Verma, J. Saroj, M. Ali and N. K. Verma, Generating a Peptide Library Using the Repeats of Amino Acid Scaffolds Created by Sliding the Framework of a 7-Mer Human Chemerin Segment and Discovery of Potent Antibacterial and Antimycobacterial Peptides, *J. Med. Chem.*, 2024, **68**(1), 566–589.

51 J. Liu, H. Li, Q. He, K. Chen, Y. Chen, R. Zhong, H. Li, S. Fang, S. Liu and S. Lin, Design, Synthesis, and Biological Evaluation of Tetrahydroquinoline Amphiphiles as Membrane-Targeting Antimicrobials against Pathogenic Bacteria and Fungi, *Eur. J. Med. Chem.*, 2022, **243**, 114734.

52 S. Gupta, V. Luxami and K. Paul, Unlocking the Antibacterial Potential of Naphthalimide–Coumarins to Overcome Drug Resistance with Antibiofilm and Membrane Disruption Ability against Escherichia Coli, *ACS Appl. Mater. Interfaces*, 2025, **17**(3), 4380–4399.

53 J. Zhang, N. Battini, J.-M. Ou, S.-L. Zhang, L. Zhang and C.-H. Zhou, New Efforts toward Aminothiazolylquinolones with Multitargeting Antibacterial Potential, *J. Agric. Food Chem.*, 2023, **71**(5), 2322–2332.

54 X. Lu, X. Xu, Y. Ding, X. Gong, L. Ming, X. Dai, C. Gu, J. Wang, J. Zhao and M. Gao, Discovery and Optimization of Tetrahydroacridine Derivatives as a Novel Class of Antibiotics against Multidrug-Resistant Gram-positive Pathogens by Targeting Type I Signal Peptidase and Disrupting Bacterial Membrane, *Eur. J. Med. Chem.*, 2025, **283**, 117101.

55 F. He, X. Liu, S. Yang, H. Tan, L.-P. Yang and L.-L. Wang, Guanidinium-Functionalized Carbon Dots: An Efficient Antibacterial Agent against Multidrug-Resistant ESKAPE Pathogens, *ACS Appl. Mater. Interfaces*, 2024, **16**(48), 65955–65969.

56 R. Yang, W. Cheng, M. Huang, T. Xu, M. Zhang, J. Liu, S. Qin and Y. Guo, Novel Membrane-Targeting Isoxanthohumol-Amine Conjugates for Combating Methicillin-Resistant Staphylococcus Aureus (MRSA) Infections, *Eur. J. Med. Chem.*, 2024, **268**, 116274.

57 Y.-F. Sui, M. F. Ansari, B. Fang, S.-L. Zhang and C.-H. Zhou, Discovery of Novel Purinylthiazolylethanone Derivatives as Anti-Candida Albicans Agents through Possible Multifaceted Mechanisms, *Eur. J. Med. Chem.*, 2021, **221**, 113557.

58 S. Roy, A. Mondal, V. Yadav, A. Sarkar, R. Banerjee, P. Sanpui and A. Jaiswal, Mechanistic Insight into the Antibacterial Activity of Chitosan Exfoliated MoS2 Nanosheets: Membrane Damage, Metabolic Inactivation, and Oxidative Stress, *ACS Appl. Bio Mater.*, 2019, **2**(7), 2738–2755.

59 S. Gupta and K. Paul, DNA Damage and Intercalation by Elinafide Modified Bis-Naphthalimides for Their Anticancer Activity, *J. Mol. Liq.*, 2023, **382**, 121980.

60 S. Gupta, V. Luxami and K. Paul, Deciphering Binding Potential of Naphthalimide–Coumarin Conjugate with c-MYC G-Quadruplex for Developing Anticancer Agents: A Spectroscopic and Molecular Modeling Approach, *ACS Appl. Bio Mater.*, 2025, **8**(2), 1077–1096, DOI: 10.1021/acsabm.4c01388.

61 P. Sharma and K. Paul, Selective Recognition of Oncogene Promoter C-Myc G-Quadruplex: Design, Synthesis, and In Vitro Evaluation of Naphthalimide and Imidazo[1,2-a]Pyrazines for Their Anticancer Activity, *ACS Appl. Bio Mater.*, 2025, **8**(2), 1377–1396.

62 P. Sarkar, S. Gupta, A. H. Udaya Kumar, D. Das, S. Sutradhar, K. Paul, N. K. Lokanath and B. N. Ghosh, Protein Interactions and Drug Displacement Studies of Novel Copper(II) and Zinc(II) Complexes of a Dipyrazinylpyridine Ligand, *J. Mol. Liq.*, 2023, **387**, 122561, DOI: 10.1016/j.molliq.2023.122561.

63 S. Gupta, V. Luxami and K. Paul, Bacterial Cell Death to Overcome Drug Resistance with Multitargeting Bis-Naphthalimides as Potent Antibacterial Agents against Enterococcus Faecalis, *J. Mater. Chem. B*, 2024, **12**(23), 5645–5660.

64 S. Rani, S. Gupta, V. Luxami and K. Paul, A Novel Target and Biomarker Benzothiazolyl–Naphthalimide Probes for Precise and Selective Detection of Serum Albumin and Anticancer Activity, *New J. Chem.*, 2022, **46**(25), 12082–12092, DOI: 10.1039/D1NJ03650E.

65 CCDC 2424188: Experimental Crystal Structure Determination, 2026, DOI: 10.5517/ccdc.csd.cc2mckm6.